Direct measurements of the 3D plasma velocity in Single-Helical-Axis RFP plasmas

J. Boguski,[1, a)] M. D. Nornberg,[2] U. Gupta,[1] K. J. McCollam,[1] A. F. Almagri,[1] B. E. Chapman,[1] D. Craig,[3] T. Nishizawa,[1] J. S. Sarff,[1] C. R. Sovinec,[1, 2] P. W. Terry,[1] and Z. A. Xing[1]
[1)] *Department of Physics, University of Wisconsin - Madison, Madison, Wisconsin 53706, USA*
[2)] *Department of Engineering Physics, University of Wisconsin - Madison, Madison, Wisconsin 53706, USA*
[3)] *Department of Physics, Wheaton College, Wheaton, Illinois 60187, USA*

(Dated: 17 November 2020)

The first local velocity measurements of helical equilibrium plasmas in the Reversed Field Pinch (RFP) Single Helical Axis (SHAx) state using a Charge Exchange Recombination Spectroscopy (CHERS) diagnostic are presented. Measurements show strong axisymmetric and non-axisymmetric flow, with $n = 5$ components of flow related to the $(m,n) = (1,5)$ dominant magnetic mode on the order of the axisymmetric flow in certain regions of the plasma, as well as significant $n > 5$ flow. Flow measurements are compared with NIMROD simulations of visco-resistive, single-fluid MHD in toroidal and cylindrical geometries with limited axial periodicity. Both measurements and the simulation with toroidal geometry show stronger inboard flows relative to the outboard flows, which is attributed to the toroidal geometry of the device. In the experiment, the $n = 5$ component of flow is phase shifted from the reconnection-like flow pattern observed in the single-fluid simulations, possibly due to decoupling of the ion and electron fluids over much of the plasma. Finally, the strength of the helical angular flow shear relative to the critical shear necessary to disrupt nonlinear coupling between tearing modes is calculated around the helical magnetic axis. The shear in the measured flow is on the order of the theoretical critical threshold needed to nonlinearly decouple modes, but the measurement uncertainty in the gradient of the flow is large.

I. INTRODUCTION

Self-organized, non-axisymmetric plasma dynamics that have potentially useful features for fusion concepts can be present in toroidal plasmas. In the plasma boundary, resonant magnetic perturbations (RMPs) are used to deform the boundary in order to mitigate Edge Localized Modes (ELMs)[1]. Plasma flow has been shown to stabilize resistive wall modes[2]. Islands produced by external magnetic perturbation coils in LHD can induce spontaneous flow and flow shear in the plasma[3]. The same device has shown that magnetic stochastization of the plasma causes flow damping[4]. Plasma discharges with a long-lived non-axisymmetric core have been created in DIII-D[5], ASDEX[6], MAST[7], TCV[8], JET[9], and are planned for ITER[10,11]. In the reversed field pinch (RFP), the plasma is sustained through a dynamo process of interacting magnetic and flow perturbations. A long-lived, self-organized helical equilibrium can arise in an RFP plasma with improved confinement properties[12]. Magnetic and flow fields interacting to produce self-organization via nonlinear MHD processes underlies many of these features. Understanding the details of non-axisymmetric plasma self-organization relies on characterizing many aspects of the plasma. This work focuses on the first characterization of the local ion flows in a self-organized helical RFP equilibrium.

The RFP has a safety factor profile $q < 1$ that peaks on or near the magnetic axis and passes through zero at or near the plasma edge, causing it to contain many poloidal $m = 1$ and toroidal n tearing mode resonant surfaces at different radii[13]. Typically only one or two of the innermost tearing modes are unstable, but a wide spectrum of modes is observed due to nonlinear interactions between the modes[14]. For standard RFP discharges, the tearing modes have comparable amplitude. The resulting island widths overlap leading to a high degree of magnetic stochasticity, which degrades energy and particle confinement in the plasma. Under certain conditions the innermost tearing mode can grow to large amplitude such that the magnetic energy in the mode is much greater than the energy in all other tearing modes combined. This situation is referred to as Quasi-Single Helicity (QSH)[15], and we will refer to the kink-tearing mode that is larger than all the rest as the dominant mode. Within the QSH condition, if the dominant mode is sufficiently strong, the core region attains a helical magnetic axis, analogous to stellarator configurations. The change in magnetic topology results in a reduction in magnetic stochasticity leading to regions of plasma with better energy and particle confinement[16]. The resulting plasma is referred to as the Single Helical Axis (SHAx) state[17,18].

Measurements of ion velocities are critical to understand the nonlinear processes that generate the SHAx state and for fully characterizing the plasma in general. This paper presents the first measurements of local ion velocities in the saturated SHAx state. Previous measurements of flows in the QSH state have been made, but they either use passive, line-integrated measurements and infer local velocities using simulation results[19–21], or they measure a growing QSH mode that did not saturate[22]. Based on the local measurements reported here for plasmas in the Madison Symmetric Torus (MST) device, commentary is made regarding the effect of the toroidal geometry, two-fluid physics, and flow shear on the plasma.

a)Electronic mail: jboguski@lanl.gov; Currently located at Los Alamos National Laboratory, Los Alamos, 87545, USA

The remainder of this paper is organized as follows: in section II, we discuss further background and details of the SHAx state. In section III, we describe the methods for obtaining the novel localized flow measurements in a self-organized, non-axisymmetric state. In section IV we present the flow data and make observations by analyzing a parameterized profile of the flow data. In section V, we present NIMROD simulations of a SHAx state and compare them to the experimental data. In section VI, we comment on the effects of the toroidal geometry of the device and two-fluid physics on the flow profiles, as well as provide an analysis of the helical angular shear flow measured in the plasma. Finally, in section VII we summarize the results and comment on the impact of the work.

II. THE SATURATED SHAX STATE

It is important to distinguish between QSH, SHAx, and a regime we refer to as the saturated SHAx state. As mentioned earlier, QSH describes the relative distribution of magnetic mode energy in the plasma, whereas SHAx indicates that the average flux surfaces that best describe the plasma are helical as opposed to axisymmetric. The QSH state in an RFP is often characterized using the spectral index of the plasma, defined as

$$N_{\mathrm{s}} = \left[\sum_n \left(\frac{\tilde{b}_n^2}{\sum_{n'} \tilde{b}_{n'}^2} \right)^2 \right]^{-1}, \tag{1}$$

where $\tilde{b}_n$ is the perturbed magnetic field amplitude of a given tearing mode with toroidal mode number n[23]. The summation in MST ranges from $n = 5$ to $n = 15$, where $n = 5$ is the lowest order tearing mode, and the mode energy for $n > 15$ modes is small. The plasma is considered to be in the QSH state when $N_{\mathrm{s}} < 2$. Since the SHAx condition is a statement of the internal magnetic topology of the plasma, it is difficult to precisely identify when the transition to SHAx occurs. The plasma is estimated to enter the SHAx state when the dominant mode amplitude is $\frac{|b_D|(a)}{B_0(a)} = 2-4\%$, where $|b_D|(a)$ is the perturbed magnetic field matching the helicity of the dominant mode at the wall, and $B_0(a)$ is the axisymmetric field measured at the wall[24]. In most cases, the dominant mode continues to grow beyond this level. In MST, the RFP used for this work, the dominant mode will not saturate until it reaches 6-9% of the edge magnetic field, well above the threshold for entering the SHAx state. MST plasmas in this regime have previously been characterized as having helical density profiles[18], temperature profiles[25,26], soft x-ray emissivity[27], and hard x-rays from a confined fast election population[25], all indicating the plasma is in a SHAx state. The helical equilibrium is maintained at this level in a relatively steady-state condition. Figure 1 shows the time series of magnetic toroidal mode amplitudes measured at the device wall during a plasma discharge that reaches a saturated SHAx state at 26 ms.

Before entering the QSH state and subsequent saturated SHAx state, the plasma is in a multi-helicity (MH) state, where all the tearing modes are of comparable amplitude and $N_{\mathrm{s}} > 2$. The transition between an MH plasma and a saturated

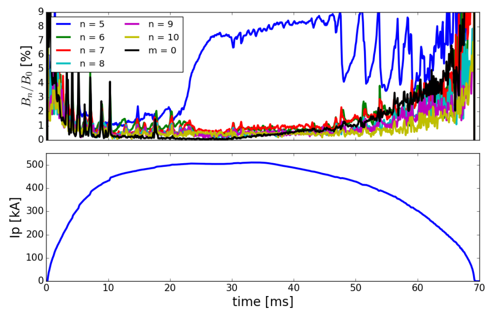

FIG. 1. Example of a long lived QSH discharge in MST. Top: The tearing mode amplitudes measured at the wall,B_n, are normalized to the equilibrium magnetic field measured at the wall, B_0. The $n = 5$ tearing mode amplitude dominates over the other, higher n tearing modes in MST non-reversed plasmas that are used for this work. Bottom: Plasma current evolution. The saturated SHAx state in this discharge begins at approximately 26 ms, and the plasma is in the multi-helicity state before 21 ms.

SHAx plasma is typically quick relative to the total plasma discharge time. The two states can be thought of as two poles in a chaotic attractor system, and the amount of time spent at either pole is influenced by the plasma Lundquist number,

$$S = \frac{\mu_0 L V_{\mathrm{A}}}{\eta} \sim \frac{T_{\mathrm{e}}^{3/2} I_{\mathrm{p}}}{\sqrt{n_{\mathrm{i}}}}, \tag{2}$$

where L is the characteristic system length, V_{A} is the Alfvén speed, η is the resistivity, T_{e} is the electron temperature, I_{p} is the plasma current, and n_{i} is the ion density. Empirically, higher Lundquist number non-reversed plasmas that have vanishing toroidal field at the plasma surface $B_\phi(a) = 0$, are more likely to enter, and stay in, the SHAx state[28,29]. Plasma discharges for this dataset are non-reversed, operated at relatively high Lundquist number ($S \sim 10^6$)[29], and spend much more time in the saturated SHAx state than the multi-helicity or transition states, as indicated by the colorscale in Figure 2. In these conditions, the plasma spent 4.5 times longer in the saturated SHAx state than in the MH state between in the interval from 5 ms to 45 ms after the start of the discharge. Plasma discharges run at a lower plasma current would spend more time in the MH state.

III. DIAGNOSTICS AND DATA ANALYSIS METHODOLOGY

As mentioned, the data for this work was obtained on the Madison Symmetric Torus (MST)[30], which produces RFP plasmas with a minor radius of $a = 0.50$ m and a major radius of $R = 1.5$ m. MST has a 5 cm thick aluminum shell that provides a conducting boundary for the plasma as well as a poloidal and toroidal ring of carbon limiters to mini-

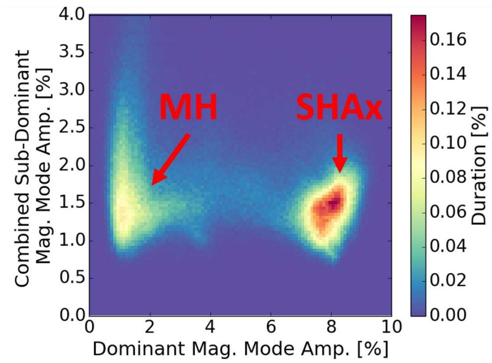

FIG. 2. 2D Histogram of 1445 non-reversed 500 kA discharges at $\langle n_e \rangle \sim 0.5 \times 10^{12}$ cm^{-3}. The horizontal axis is the dominant magnetic tearing mode amplitude measured at the wall, the vertical axis is the combined sub-dominant tearing mode amplitudes. Each pixel represents a unique histogram bin, where a magnetic measurement with exposure time of 0.1 ms is equivalent to one count. The color scale represents the number of measurements made at that pixel's location normalized by the total number of measurements made in the dataset, which is inferred as the duration of time an average SHAx plasma discharge is at that histogram location. The histogram shows that discharges at this current and density spends a large percentage of the time in the SHAx state as opposed to the multi-helicity (MH) state.

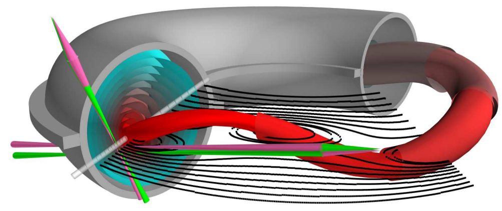

FIG. 3. SHAx plasma with both CHERS optical views (toroidal and poloidal) and neutral beam (gray). The two light cones (green and purple) represent the off-beam and on-beam views respectively for both poloidal and toroidal CHERS views. The black lines show the intersection of representative flux surfaces obtained by V3FIT with the plane that would be sampled by the neutral beam as the plasma is rotated through the beam.

mize plasma interaction with the aluminum wall. The plasmas used for this paper were run in a non-reversed mode, the plasma current was $I_p = 500$ kA, and the plasma density was $\langle n_e \rangle \sim 0.5 \times 10^{12}$ cm^{-3}. When MST is operated in non-reversed mode, the applied toroidal field is exactly zero. The likelihood of entering a QSH state is higher in non-reversed plasmas[18]. One possible reason is that the resonant surface for $m = 0$ is removed from the plasma, suppressing three-wave nonlinear mode coupling with $m = 1$ modes. The dominant mode in MST non-reversed plasmas is the $(m,n) = (1,5)$ mode. The amplitude and phase of tearing modes are measured using a toroidal array of magnetic diagnostic coils located on the inside surface of MST's aluminum shell. The remainder of this section will discuss the details of how localized, averaged, absolute velocity measurements were made in the saturated SHAx state.

Ion velocity measurements are made using the Charge Exchange Recombination (CHERS) diagnostic[31,32]. The custom spectrometer is used to measure the Doppler shift of 343.383 nm light from the C^{+5} $n = 7 \rightarrow 6$ transition emitted from charge exchange between fully stripped C^{+6} and a neutral hydrogen beam. To isolate the charge exchange emission from MST's substantial background signal, two views are used for any one spatial location: one with its focus at the neutral beam, and another slightly displaced view whose focus is to the side of the beam so that it observes only background emission. Together the two views are able to isolate the emission from charge exchange alone by forward modelling the light for each view using a common set of background parameters. The background light in this spectral range is dominated by electron impact emission from O^{+5} and C^{+5}. It is unclear at these temperatures which element dominates the background emission, but the modelled charge exchange signal tends not to be affected by the choice of background element[33].

The spectrometer supports two fiber inputs, so only one spatial location can be measured at a time. The light can be observed from one of two orientations, toroidal or poloidal, both of which are perpendicular to the neutral beam. The 50 keV hydrogen neutral beam has an average diameter of 4 cm and extends radially through the plasma, passing through the axisymmetric Shafranov-shifted magnetic axis under non-SHAx conditions. The neutral beam is for diagnostic purposes, and it has low enough density that there is little perturbative effect on the plasma. The intersection of the neutral beam and optical views provides localization of the charge exchange measurement. The measurement region extends through the diameter of the neutral beam, has a radial extent of 1 cm for the poloidal view, and has a 2 cm radial extent for the toroidal view. Figure 3 shows a typical SHAx plasma with the neutral beam (gray), and both CHERS optical views (purple and green) displayed for both orientations (poloidal and toroidal). The shape of the plasma shown in the figure is based on the magnetic equilibrium in the saturated SHAx state, obtained from V3FIT reconstructions of MST plasmas[26,34], which assumes nested flux surfaces. The black lines in Figure 3 show representative flux surfaces that would be sampled by the neutral beam as the plasma is rotated through it for 1/5 of the torus. These flux surfaces are used later as a reference in Figure 5, which provides a 2D plot of velocity contours with overlaid flux surfaces.

The optical views can be moved along the neutral beam to provide radial resolution of the flow measurements. There are viewing ports directly above the neutral beam, spaced 8.9 cm apart, that provide a perpendicular view to the beam to measure poloidal flow. The axis for poloidal flow is chosen to be where the neutral beam intersects the mid-plane, which would be the location of the Shafranov-shifted magnetic axis in MH conditions. The magnetic axis under MH conditions

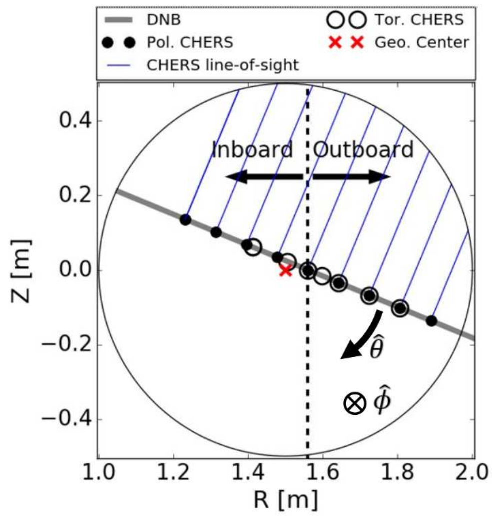

FIG. 4. Poloidal cross-section of MST indicating location of neutral beam (gray line), poloidal velocity measurement locations (closed circles), and toroidal velocity measurement locations (open circles). The axis for poloidal flow measurements is chosen to be where the neutral beam crosses the mid-plane, 6 cm to the right of the geometric center (red "x"), approximately the location of the axisymmetric Shafranov-shifted magnetic axis in non-SHAx conditions, and the axis the new helical magnetic axis revolves around.

have been calculated using MSTFIT[35]. The new helical magnetic axis revolves about this axisymmetric axis as it is traced out in toroidal angle. There is one large viewing port for the toroidal view which allows data to be collected anywhere between 16 cm inboard and 26 cm outboard along the neutral beam. The radial locations of the poloidal and toroidal measurements used in this paper are displayed in Figure 4.

For most QSH plasmas, and all 500 kA SHAx plasmas that saturate, the plasma locks early in the discharge, well before saturation occurs. The plasma stability is not appreciably affected by locking, but it complicates the ability to obtain velocity measurements with toroidal spatial resolution, which is typically done by measuring the velocity in time as the plasma rotates through the neutral beam. While standard RFP plasmas naturally spin up[36], the locking in SHAx states is caused by a braking torque localized to the tearing mode's resonant surface that scales with the strength of the tearing mode perturbation[37]. The locking orientation of the helical equilibrium can be controlled, however, using a resonant magnetic perturbation (RMP) system that consists of 38 coils which apply a radial magnetic field at a single toroidal location in MST[25]. The plasma still remains locked for the duration of a discharge, but toroidal resolution is obtained by changing the locking orientation every shot. The plasma is essentially rotated through the neutral beam on a shot-by-shot basis. The RMP is used for the majority of this dataset and has an estimated $n = 5$ mode strength of 1-2% of the edge magnetic field, which has been shown to have no substantial effect on QSH confinement[38]. Even so, the RMP is only applied during QSH onset and is turned off before the plasma reaches the saturated SHAx state.

For each shot, the location of the flow measurement relative to the helical equilibrium is inferred from the phase of the dominant mode measured by the toroidal array of magnetic diagnostic coils at the edge of plasma. The phase measurement maps 1:1 to a toroidal angle of the helical equilibrium, ϕ_{SHAx}, used later in the text. By using the phase measurement, an assumption is made that the helical equilibrium has a toroidal $n = 5$ periodic symmetry, consistent with the presence of a large, saturated $(m,n) = (1,5)$ mode. Furthermore, this assumption has successfully been used in V3FIT reconstructions of MST[26] which yielded synthetic diagnostic results that closely matched actual measurements.

The average flow in the saturated SHAx state is measured by aggregating all flow measurements in time and over multiple discharges made at the same $n = 5$ locking phase. Since the measurements are averaged over a time much longer than the carbon-deuterium collision time, the flow measurements are considered to be representative of the bulk deuterium velocity as well. The presence of an ion specific momentum drive or loss is not considered here. There is good shot-to-shot agreement in the average flow for any one measurement location, where the variance in the data is on the order of the variance due to photon statistics. The inboard flow measurements have higher variance than the outboard measurements due to attenuation of the neutral beam as it propagates from the outboard side to inboard side of the plasma.

The absolute wavelength calibration of the spectrometer performed each day allows us to know the absolute velocity to within ± 3 km/s. The calibration method, described in more detail in Craig et al.[39], leverages our ability to measure the velocity in the plasma at a location where the velocity is negligible. Such a scenario occurs when the velocity is measured in the poloidal plane at the magnetic axis of an axisymmetric plasma where poloidal current drive is used to reduce tearing mode activity[40,41]. The velocity measured at this location is used as the zero velocity baseline to calibrate the spectrometer, and this calibration was performed at the beginning and end of each day flow measurements were taken.

IV. VELOCITY PROFILES IN SHAX

In this section we present the aggregate data collected in the saturated SHAx state of 1445 SHAx discharges. Figure 5 shows the contours of the averaged poloidal and toroidal velocity on the toroidal plane sampled by the neutral beam as the plasma is rotated through it. Negative radial values on the horizontal axis of the figure indicate the inboard side of the machine, where $r/a = 0$ is measured from the point the neutral beam crosses the mid-plane. The vertical axis in the plots is the toroidal angle of the helical equilibrium, ϕ_{SHAx}. This toroidal angle is not measured relative to the machine but to the helical equilibrium that develops in the plasma for each shot. We chose as a convention in the paper to report features in terms of 5 times the toroidal angle, $-\pi < 5\phi_{\mathrm{SHAx}} < \pi$ instead of $-\pi/5 < \phi_{\mathrm{SHAx}} < \pi/5$. The zero point of ϕ_{SHAx} is chosen to be where the helical magnetic axis is in-line with the neutral beam on the outboard side, as shown by the black lines in Figure 5. The plane shown in Figure 5 is the one sampled by the plasma rotating through the neutral beam and should not be thought of as a helical flux surface.

There are many clear non-axisymmetric features in Figure 5. At $|r/a| > 0.5$ the poloidal flow varies by more than 10 km/s along the toroidal angle. The same is true for the toroidal flow at $r/a = 0.4$ and $r/a = 0.1$, where the flow nearly goes to zero at $5\phi_{\mathrm{SHAx}} \sim -3$ rad and $5\phi_{\mathrm{SHAx}} \sim 0.5$ rad respectively. It is easier to parse the axisymmetric and non-axisymmetric contributions to the flow by fitting the data to a parameterized profile consisting of a Fourier series along the toroidal angle. Since the toroidal angle enforces a 5x periodicity assumption, the modes of the Fourier decomposition are harmonics of a base $n = 5$ mode. These are harmonics correlated with the $n = 5$ helical equilibrium and are not necessarily correlated with higher order tearing mode perturbations in the plasma. The amplitudes of the modes are given in Figure 6 for the $n = 0$ mode and five harmonics of $n = 5$. Increasing the number of modes in the Fourier decomposition did not appreciably change the results for the $n \leq 25$ modes, and the amplitudes of $n > 25$ harmonics were small with uncertainty that included 0 km/s. The error bars in the reported amplitude values come from the standard deviation of fitting ten equally sized and randomly selected subsets of the total dataset.

As can be seen from Figure 6 a), the axisymmetric toroidal flow profile is a relatively uniform -9 km/s for $|r/a| < 0.5$. The toroidal flow is in the same direction as the plasma rotation before mode locking occurred, which is opposite the direction of B_ϕ and in the direction of J_ϕ. The axisymmetric poloidal flow profile has a minimum in the plasma core and solid body rotation on the inboard side ($-0.7 < r/a < 0$). On the outboard side ($r/a > 0$), flow deviates from solid body rotation, peaking at $r/a = 0.2$, and reversing direction at the outboard edge, $r/a > 0.6$. This poloidal flow reversal has been observed in previous measurements of MST plasma flows[39]. The source of asymmetry in the poloidal flow may partly be due to the toroidal geometry of the device, which will be discussed in section VI A.

Both the $n = 5$ and the $n > 5$ components of the flow shown in Figure 6 b) and c) are non-trivial in the plasma. The $n = 5$ poloidal flow is comparable to the axisymmetric flow at $r/a = -0.1$ and 0.7. The $n > 5$ poloidal flow exceeds the $n = 5$ flow at $r/a = -0.7$ and 0.5. The poloidal flow harmonic amplitudes are also indicative of solid-body rotation, with a minimum in flow at the center that increases with increasing radius. It should be noted that the poloidal flow measurement at $r/a = 0$ can be considered a radial flow according to the coordinate system presented, but it is only normal to the helical flux surfaces at $\phi_{\mathrm{SHAx}} = \pi/2$ rad and $-\pi/2$ rad. The lack of strong flow near $r/a = 0$ is similar to previous reconstructed flow profiles from line-integrated velocity measurements using simulations with a resistivity similar to the experiment[20], but different than those relying on simulations run at reduced resistivity and/or viscosity[19]. The toroidal $n = 5$ harmonic is also strong, though it never exceeds the toroidal axisymmetric flow. The toroidal $n > 5$ modes are less pronounced compared to the $n = 5$ mode, but they are still comparable to the $n > 5$ modes in the poloidal flow.

The $n = 5$ poloidal flow is broader in extent compared to previous CHERS measurements in MH and growing QSH plasmas[22], which were made in $I_{\mathrm{p}} = 400$ kA reversed RFP conditions. Previous measurements of flow associated with tearing modes in MH quiescent phase is localized near the tearing mode's rational surface. The mode velocity related to the dominant tearing mode in the growth phase of the QSH plasmas, is also broader than the MH quiescent phase, but still doesn't extend as far as the SHAx plasmas, where $n = 5$ flow is still measured at $|r/a| > 0.5$. The peak mode velocities for the SHAx plasmas are also three times that of the velocities measured in the MH quiescent phase and the dominant mode of the growing QSH phase.

V. NIMROD SIMULATION OF A QSH STATE

To better understand what physical effects are influencing the flow profiles in the SHAx state, simulations were performed to compare to experimental data. There have been several past analyses of theoretical Single Helicity (SH)[42,43] and QSH[44,45] states created in simulations. One method uses scalar viscosity and/or resistivity values much larger than the perpendicular Braginskii viscosity or Spitzer resistivity calculated from experiment to encourage the formation of a helical state by heavily dissipating the energy transferred from dominant to sub-dominant modes. A shift from MH to SH in computations is observed to depend on the plasma Hartmann number:

$$Ha = \frac{BL}{\sqrt{\eta\mu}} = \frac{S}{\sqrt{Pm}}, \tag{3}$$

where B and L are the characteristic magnetic field and length scale, η is the plasma resistivity, μ is the viscosity, Pm is the Prandtl number, and S is the Lundquist number previously defined in Equation 2. The transition from MH to SH is observed to occur when viscosity and/or resistivity increase such that the Hartmann number decreases below a threshold Hartmann number of around 2000[46].

In experimental plasmas, the Hartmann number obtained using Spitzer resistivity and perpendicular Braginskii viscosity is on the order of $Ha = 10^6$. However, the effective dissipation relevant for tearing mode interactions may be different than that implied by these estimates. For example, viscosity is enhanced above perpendicular Braginskii viscosity by stochastic fields in the nonlinear limit, an effect implied by electrode biasing experiments[47,48] and qualitatively captured in resistive-MHD simulations[49]. It is also conceivable that parallel viscosity, which is much larger and scales differently than perpendicular viscosity, might be important in the stochastic-field limit of nonlinear MHD, further increasing the effective viscosity on the tearing modes. The role of

Physics of Plasmas

AIP Publishing

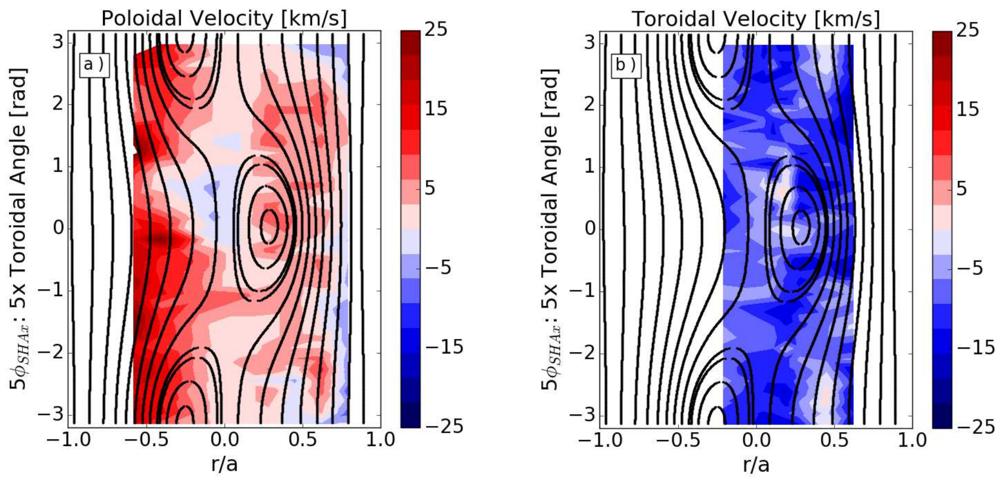

FIG. 5. a) Poloidal and b) toroidal velocity contours of averaged CHERS velocity measurements. The black lines are representative flux surfaces obtained from V3FIT. The horizontal axis is the radius measured along the neutral beam, where zero is the location the neutral beam crosses the mid-plane, $r/a < 0$ is inboard, and $r/a > 0$ is outboard. The vertical axis is the toroidal angle of the helical equilibrium, ϕ_{SHAx}, where angles are reported from $-\pi < 5\phi_{\mathrm{SHAx}} < \pi$. This figure is the same plane cut out by the plasma being rotated through the neutral beam as is shown in Figure 3.

the highly anisotropic viscosity tensor on nonlinear plasma evolution merits further investigation, though it is outside the scope of this paper.

Nonetheless, the high dissipation SH simulations also behave differently than experimental QSH plasmas. They lack significant sub-dominant modes, and the SH state persists with few of the reversions to MH that are typically observed experimentally. Furthermore, the probability of entering a QSH state is empirically observed to increase with increasing Hartmann number (based on perpendicular Braginskii viscosity), opposite the trend observed in simulations. These differences suggest the high dissipation SH simulations are in a different regime and are influenced by different mechanisms than experimental plasmas. The low Hartmann number simulations are not necessarily meant to assign a causal link between high dissipation and the formation of QSH states in experiment, but the simulations have been used to infer magnetic and flow profiles for analysis in experimental QSH plasmas[5,19]. These flow profiles include substantial $m = 1$ radial flow through the axis and poloidal flow near the axis, which are not present in the measurements made in this paper.

Another method of obtaining a QSH state is to apply an edge perturbation at the plasma boundary[45,50], which has also been successfully used in RFX-mod[51]. The process uses RFX-mod's set of magnetic perturbation (MP) coils to apply a radial magnetic perturbation of a specific poloidal and toroidal mode number on the order of 1-2% of the edge magnetic field. The simulations and experiments have shown helical regions of improved confinement matching the MP helicity. The simulations have also shown the same trend of increased QSH persistence with increasing Hartmann number that is observed experimentally. QSH states with a dominant mode that is different than the innermost tearing mode can even be created using this method. This is an interesting approach to achieving a SHAx state; however, the plasma self-organization mechanisms responsible for creating a SHAx state by continually applying an edge perturbation is likely different than the SHAx states under consideration in this paper. In contrast to applying edge perturbations, the thick aluminum shell in MST suppresses radial edge perturbations on the plasma, keeping them well below 1%. The strength of the $n = 5$ component of the RMP in MST used to encourage entry into the SHAx state and to control the locking phase of the helical equilibrium is on the order of 1-2% of the edge magnetic field, but it is only applied temporarily and is terminated before the saturation of the dominant mode occurs.

The simulations run for this work use neither high dissipation or perturbed boundary conditions to achieve a QSH state. Instead, a QSH state was obtained with a Hartmann number above the MH to QSH transition by only simulating toroidal modes that are harmonics of $n = 5$. This is equivalent to only simulating 1/5 of the torus. The poloidal spectrum is not limited other than by computational constraints. We emphasize the simulations are fully three-dimensional, only limited in toroidal harmonic content. Achieving a QSH state is attributed to the artificial elimination of tearing modes that are not harmonics of $n = 5$, such that energy is transferred away from the dominant mode less effectively and the dominant mode ampli-

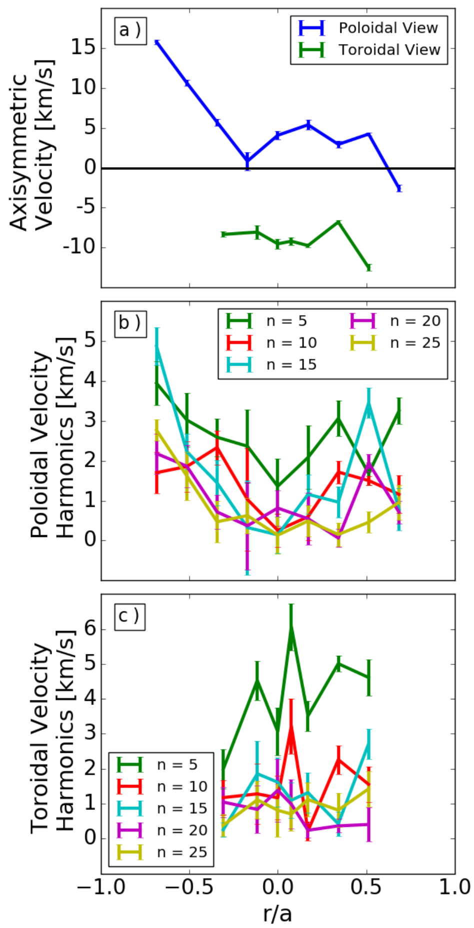

FIG. 6. a) Axisymmetric ($n = 0$) poloidal (blue) and toroidal (green) flow profiles. b) Poloidal and c) toroidal harmonic flow profiles. Error bars represent the standard deviation of the velocity amplitudes from fitting ten random subsets of the total dataset.

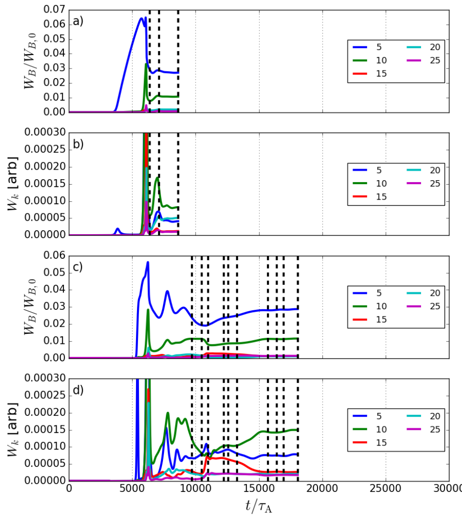

FIG. 7. Time evolution of the total magnetic mode energy, W_B, normalized by the total axisymmetric magnetic energy, $W_{B,0}$, for NIMROD simulations in a) cylindrical geometry and c) toroidal geometry as well as the total kinetic mode energy, W_k, for the b) cylindrical geometry and d) toroidal geometry. The horizontal axis expresses time normalized by the Alfvén time. The $n = 5$ magnetic mode dominates over higher n modes in a steady-state manner after an initial relaxation event, but the $n = 10$ mode dominates the kinetic energy. Dotted black lines indicate the time points used for averages in analysis of steady-state velocities.

tude is increased. Despite this limitation, the flow profiles are expected to be similar to the experimental measurements since lower resistivity and viscosity values are able to be used.

NIMROD[52] simulations are used in this paper to obtain a steady-state QSH plasma. NIMROD is an initial-value extended-MHD code that uses a 2D finite element mesh and Fourier components in the third direction. For these simulations the mesh is in R and Z and the Fourier direction is in ϕ. Two simulations are used, one run using cylindrical geometry and one run using toroidal geometry, both using 22 modes (up to $n = 105$) in a non-reversed equilibrium with an ideal conducting boundary, no slip flow boundary, and the parameters given in Table I. The Hartmann number of these simulations is 8944, well above the transition from QSH to MH observed in previous simulations. Despite this, steady-state QSH states are obtained, as shown in Figure 7, where the dominant $n = 5$ magnetic mode energy remains persistently and significantly larger than the other higher n tearing modes in time, after an initial relaxation event occurs. In the plot W_B is the total magnetic energy per mode, and W_0 is the total axisymmetric magnetic energy in the plasma. Identification of axes in the NIMROD simulation is nontrivial, and it cannot be said definitively if the simulated plasma is in a SHAx state or not. However, a helical magnetic axis can be identified from the off-axis region of healed flux surface seen in Poincaré plots, as shown in Figure 8. Even with limited periodicity of the simulations, there is significant enough mode overlap and mode interaction to cause substantial stochasticity of the plasma in both the cylindrical and toroidal geometry simulations.

In order to provide as direct comparisons as possible to

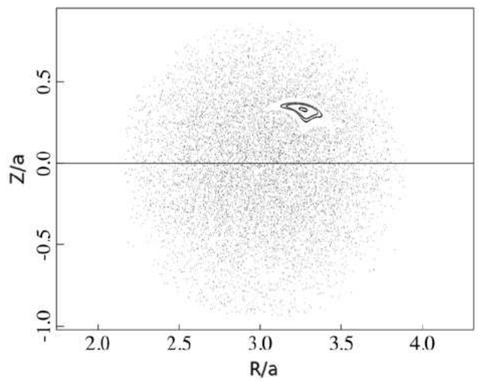

FIG. 8. Poloidal cross-section of the toroidal geometry NIMROD simulation Poincaré plot at $5\phi_{\mathrm{SHAx}} = 1.5$ rad and time point $t/\tau_{\mathrm{A}} = 18069$ showing the region of healed flux surfaces.

Parameter	Value
Boundary Condition:	Periodic, $N = 5$
Hartmann #:	8944
Lundquist #:	4×10^{4}
Magnetic Prandtl #:	20
Resistivity:	$2.5\times10^{-5}(1+9r^{30})^{2}$
Viscosity:	5×10^{-4}
Thermal Conduction:	Isotropic
β:	0.01%
R_0/a	3.0

TABLE I. Relevant NIMROD simulation run parameters.

experimental measurements, NIMROD ion velocities are reported at locations and lines of sight that match those obtained from the CHERS diagnostic in the experiment. However, the poloidal axis in NIMROD is in a different location than the experiment due to different amounts of Shafranov shift. To properly match the experimental and simulated velocity measurements, the line of velocity measurements along an imagined neutral beam in NIMROD is shifted to intersect the poloidal axis for each simulation. For the cylindrical simulation, this means that the "neutral beam" intersects the mid-plane at the geometric center.

The velocities used are in non-dimensionalized units relative to the Alfvén speed, with $V_{\mathrm{A}} = 1$. Since the simulations are run at a different Lundquist number than the experiment, the simulation cannot be scaled to match the machine parameters for both Alfvénic times and resistive times. Scaling the simulation velocity by the experimental Alfvén velocity to match Alfvénic timescales would cause the resistive diffusion timescales between the simulation and experiment to be off by the ratio of the Lundquist numbers. A scaling that is a compromise between the two timescales is chosen:

$$V_{\mathrm{scaled}} = V_{\mathrm{NIM}} * V_{\mathrm{A,MST}} \sqrt{\frac{S_{\mathrm{NIM}}}{S_{\mathrm{MST}}}}, \tag{4}$$

where V_{NIM} is the normalized velocity reported by NIMROD, $V_{\mathrm{A,MST}}$ is the Alfvén velocity of the experimental MST plasmas (10^6 m/s), S_{NIM} is the Lundquist number of the NIMROD simulation, and S_{MST} is the Lundquist number of the experimental MST plasmas (10^6). This scaling is motivated by the resistive tearing mode growths rates that lie between Alfvénic and resistive timescales. However, it is only an estimate, and simulations run at the same parameters as the experiment would be necessary to more accurately compare flow magnitudes. Given the simplifications used in the computation, it is not expected that the velocities will match the experimentally measured values, but it is expected they should reach the appropriate order of magnitude.

Cross-sections of poloidal and toroidal flow matching the cross-section measured in the experiment are shown in Figure 9 for both the cylindrical and toroidal geometry simulations. The mechanisms that drive net axisymmetric plasma flow in MST plasmas are not adequately simulated in resistive-MHD computations, so visual comparison between the two simulation and experimental figures is limited. What can be seen from the figures in Figure 9 is that the strength of the perturbations is larger for $r/a > 0.5$ than $r/a < 0.5$, as in the experimental measurements. The typical flow pattern is further characterized in Figure 10, showing the full flow profile for a poloidal cross-section for the toroidal geometry simulation at $t/\tau_{\mathrm{A}} = 18069$ and $\phi_{\mathrm{SHAx}} = 1.5$ rad, the same toroidal location as the Poincaré plot in Figure 8. Since experimental data is only taken at one poloidal location, the poloidal cross-section of flow cannot be easily compared to the flow in the experiment. Such a comparison would require relying on a model for reconstructing flow in the poloidal plane which makes assumptions about the poloidal mode content of the flow and would not be well constrained by the experimental data.

The flow profiles between the experimental data and the simulation data is most easily compared by considering the mode amplitudes of the flow. The poloidal flow profiles for both the cylindrical and toroidal geometry simulations are qualitatively similar to the experimental measurements, as can be seen in Figure 11 a) and b). Specifically, there is an overall rotational profile with a minimum at $r/a = 0$ and amplitudes that increase with increasing radius as well as significant contributions from $n > 5$ modes. The amplitude of the $n > 25$ modes are small compared to the $n \leq 25$ modes and are not shown. The profiles shown in Figure 11 are averaged from the time points in the simulation indicated in dotted black lines in Figure 7, and the error bars represent the standard deviation of the data. The poloidal flow shows a strong $n = 10$ flow in both simulations, especially at larger radii. This is attributed to a strong $(m,n) = (1,10)$ tearing mode. The strength of the mode and the fact that it is present at larger radius also explains why the global kinetic energy in the plasma is dominantly $n = 10$, as shown in Figure 7 b) and c). The toroidal velocity profile is significantly different in the simulations compared to the experiment, however. Comparing to Figure 6 c), the NIMROD simulations have very weak non-axisymmetric toroidal flow at the center of the plasma, where the experimental measurements for toroidal flow show substantial non-

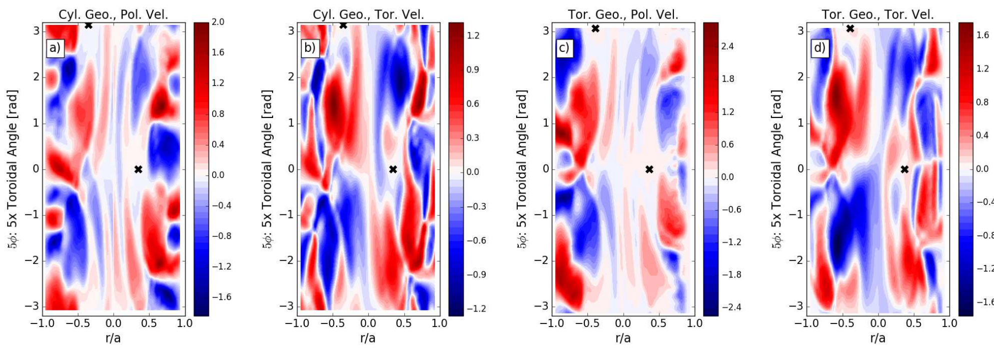

FIG. 9. Perturbed velocity contours in NIMROD simulations at the same poloidal location as the experimental CHERS measurements in 5. Figures a) and b) are the poloidal and toroidal velocities in cylindrical geometry respectively, and figures c) and d) are the poloidal and toroidal velocity in toroidal geometry respectively. The data shown is for a single time point from the simulations, $t/\tau_A = 18069$ for the toroidal geometry simulation and $t/\tau_A = 8631$ for the cylindrical geometry simulation. The black 'x' in the figures represents the estimate of the helical axis location.

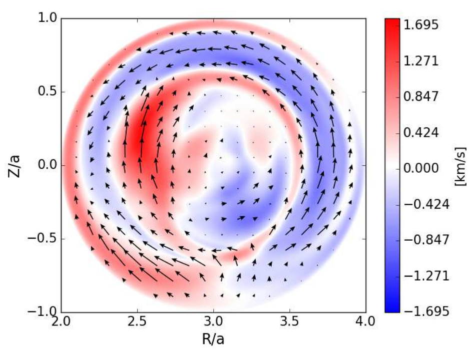

FIG. 10. Poloidal cross-section of the toroidal geometry NIMROD simulation showing velocity at $5\phi_{\text{SHAx}} = 1.5$ rad and time point $t/\tau_A = 18069$. The black arrows show the direction of velocity in the poloidal plane, with the length of the arrow representing the relative strength of the flow, and the color scale represents the toroidal velocity.

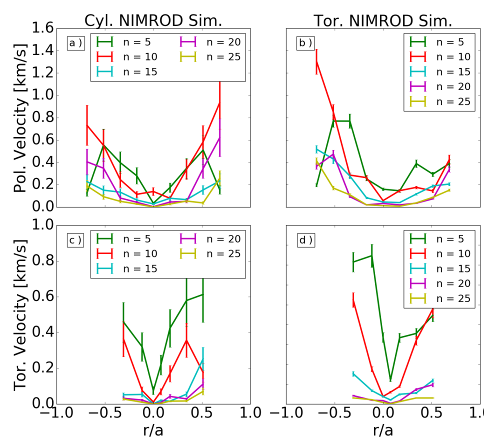

FIG. 11. Average NIMROD velocity mode amplitudes from the time points shown in the dotted black lines in Figure 7 at the same radial locations and orientations as the CHERS diagnostic in MST. Poloidal and toroidal flow is provided in a) and c) respectively for the cylindrical geometry simulation and b) and d) respectively for the toroidal geometry simulation. Error bars represent the standard deviation of velocity amplitude used in the averages.

axisymmetric flow. The decrease in non-axisymmetric flow observed in the inboard side of the experimental toroidal flow is also not observed in the simulation. The NIMROD velocity amplitudes overall are about five times weaker than the measured values. This is not surprising given the missing physics (i.e. two-fluid, significant beta, diamagnetic flow, and lower viscosity). Since the $n = 0$ axisymmetric flow is not expected to match the experiment, it is not reported in Figure 11.

Simulations were also run with high dissipation by increasing the Prandtl number form 20 to 2000, giving a Hartmann number of $Ha = 894$. The simulations were run in toroidal geometry for a simulation of 1/5 of the torus and a simulation of the entire torus. Both simulations produced a QSH state, as shown in Figure 12. The simulation of only 1/5 of a torus produced a strong $n = 5$ magnetic mode that was consistently dominant, but oscillated strongly in time, never reaching a steady-state. The simulation of the entire torus produced a strong $n = 5$ dominant mode that gave way later in time to

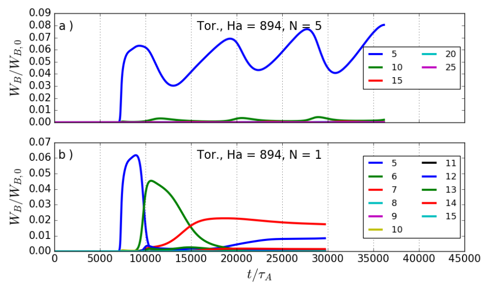

FIG. 12. Time evolution of the total magnetic mode energy, W_B, normalized by the total axisymmetric magnetic energy, $W_{B,0}$, high dissipation ($Ha = 894$) NIMROD simulations in toroidal geometry for a) 1/5 of a torus ($N = 5$ limited periodicity boundary condition) and b) the entire torus ($N = 1$ periodic boundary condition). The $n = 5$ mode dominates over higher n modes, but in a) the mode oscillates strongly and in b) other modes rise up to become dominant.

an $n = 6$ mode and then an $n = 7$ mode, and it ended perhaps before nonlinear evolution was fully settled. The behavior of flow profiles in these simulations was complex and not straightforwardly comparable to experiment. Since neither the magnetic mode energies nor the flow profiles match the experimental observations well in either simulation, they are not considered further in VI.

.

VI. DISCUSSION

The experimental velocity measurements along with the low dissipation NIMROD simulations can be used to infer more about the impact of certain physical effects on the plasma. Specifically, in this section the effects from the toroidal geometry and two-fluid effects on the velocity measurements are considered. The section will conclude with a characterization of a component of velocity shear, a quantity hypothesized to play an important role in the formation and sustainment of the QSH state[53].

A. Toroidal effects on flow profiles

The influence of the toroidal geometry can be seen by comparing flow profiles between cylindrical and toroidal simulations in Figure 11, where inboard/outboard flow asymmetries are present in the toroidal simulation. The experimental results for the poloidal flow in both the axisymmetric flow and the non-axisymmetric flow harmonics show clear inboard/outboard asymmetries, where the inboard flow is stronger than the outboard flow. The toroidal flow measurements do not extend far enough on the inboard side to draw any conclusions as to the effect of the toroidal geometry on toroidal flow.

A simple analysis of the poloidal flow can help characterize the strength of the flow asymmetry. Since the measurement points are equidistant from the poloidal axis, the ratio of the total inboard poloidal flow and the total outboard poloidal flow can be used to get a basic quantification of the inboard/outboard flow asymmetry. The ratio is

$$F_{\mathrm{IN/OUT}} = \frac{\sum_{R_{\mathrm{IN}}=[R_{\mathrm{CHERS,inboard}}]} V_n(R_{\mathrm{IN}})}{\sum_{R_{\mathrm{OUT}}=[R_{\mathrm{CHERS,outboard}}]} V_n(R_{\mathrm{OUT}})}, \qquad (5)$$

where $[R_{CHERS,inboard}]$ is the set of inboard CHERS locations, $[R_{CHERS,outboard}]$ is the set of outboard CHERS locations, and V_n is the n toroidal mode velocity. A device without toroidal geometry effects is expected to have a poloidally symmetric flow profile, and the ratio would be one. A deviation from unity is attributed to the toroidal geometry of the system. The ratio of flow for each harmonic of the parameterized profile of poloidal flow for the experimental data, the cylindrical NIMROD simulation, and the toroidal NIMROD simulation is shown in Figure 13. It is clear from Figure 13 that both the experiment and toroidal NIMROD data have flow ratios greater than one, where the cylindrical simulation stays at a ratio of one, as expected.

Greater inboard flow relative to the outboard is not surprising, if an incompressible flow and flat density profile is assumed, since the total volume on the inboard side is less than the outboard. The ratio of cross-sectional area between the inboard and outboard sides of MST would give an expected ratio between inboard and outboard velocity of $F_{\mathrm{IN/OUT}} = 1.4$. This simple geometrical factor would account for the asymmetry in most of the non-axisymmetric flow in the experiment. The stronger ratio for the axisymmetric flow on the inboard side may be due to a stronger flow drive on the inboard side. The toroidal geometry simulation has an inboard to outboard flow ratio larger than 1.4. The specific mechanisms causing this are unclear and likely complex, but since the only change between the two simulations is the geometry, it clearly stems from the influence of the toroidal geometry.

B. Two-fluid effects in the saturated SHAx state

The NIMROD simulations were run using single-fluid MHD. However, two-fluid effects are likely important in the MST core[54], and have been measured experimentally during sawtooth crashes in MH plasmas[55]. In single-fluid, resistive MHD (or two-fluid MHD with cold ions), the ion and electron flows associated with a magnetic island form convective cells out-of-phase with the island structure, where there is inflow at the x-point and outflow at the O-point. When ions are warm and the motions of the ions and electrons begin to decouple, the electron flow responsible for advecting flux into the island will remain unchanged, but the global ion flow profile will shift along the helical angle of the island such that the ion convective cells are no longer out-of-phase with the island structure[56].

The convective cells associated with an island consists of a radial and helical flow. There are no experimental radial flow

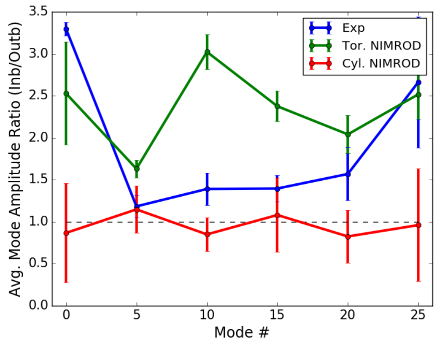

FIG. 13. Ratio of inboard/outboard poloidal flow per toroidal mode number for experimental data and the cylindrical and toroidal NIMROD simulations using the CHERS synthetic diagnostic. A ratio greater than one implies greater inboard flow than outboard flow, where a simple incompressible, uniform density plasma assumption in MST would have an expected ratio of 1.4 due to the toroidal geometry of the device.

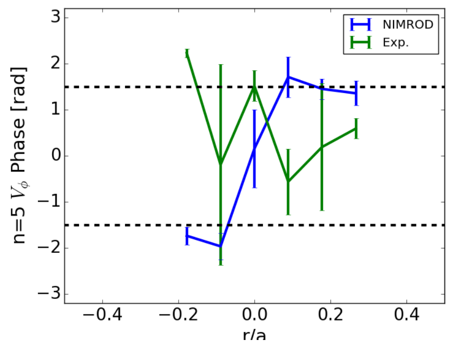

FIG. 14. Phase of the helical flow for the experimental data (green) and the toroidal NIMROD simulation (blue). A phase of $\pm\pi/2$ indicates the flow extremum is out-of-phase with the helical magnetic axis, as would be predicted from single-fluid MHD. A phase shift away from $\pm\pi/2$ is indicative of a decoupling of the ion and electron fluid.

measurements available to reconstruct the full global flow profile, but the helical flow ($V_\chi = mV_\theta + nV_\phi$) can be reconstructed at locations where the poloidal and toroidal measurements sufficiently overlap, within $-0.2 < r/a < 0.45$. The phase of the flow perturbation relative to the toroidal angle can then be extracted. For single-fluid MHD, the helical flow profile measured along a toroidal angle centered at the tearing island axis should be $\pm\pi/2$ relative to the axis. A shift away from that peak is indicative of a decoupling of the electron and ion fluid.

Figure 14 shows the phase of the helical flow for the experimental measurements and the NIMROD simulation with toroidal geometry. The NIMROD simulation data shows good agreement with the expected single-fluid flow pattern; however, the experimental data differs from the single-fluid expectation. This is attributed to the effect of the two-fluid physics in the experimental plasma. This measurement is only an inference, since it is unclear exactly what the SHAx flow pattern in the experimental parameter regime should look like. Future two-fluid, toroidal SHAx simulations would improve the ability to interpret experimental data.

C. Flow shear of in the saturated SHAx state

It has been suggested that the mechanism responsible for producing the QSH and subsequent SHAx state in experiments is a decoupling of the dominant and sub-dominant modes by magnetic or flow shear[53,57,58]. Strong shear generally causes a reduction in nonlinear energy transfer in plasma turbulence by breaking apart eddies before they can transport material away from the inner plasma. For example, strong flow shear in the plasma edge is considered to be the cause of the L to H transition seen in tokamaks[59]. Peaks in flow shear have been previously measured in SH simulations as well as reconstructed experimental flow profiles and observed to exist outside the electron internal transport barrier (eITB) of helical states in RFX-mod[20,21,60].

The reduced model presented by Terry et al.[57] uses a predator-prey model to describe the interaction between dominant and sub-dominant modes and determine conditions for QSH formation and sustainment. The quantity under consideration is the shear of the helical angular velocity about the dominant mode, with a helicity matching the dominant mode. The proposed effect of this shear is demonstrated in the cartoon in Figure 15, which shows the dominant mode as an island (black lines) with a sub-dominant tearing mode "eddy" (blue lines) projected onto it. Figure 15 a) is the system without shear, and Figure 15 b) is the system with angular shear (black lines) about the tearing mode axis. For angular shear above a critical value, energy transfer from the unstable dominant mode to the sub-dominant tearing modes is suppressed, allowing the dominant mode to grow large. In the case of the SHAx state, it is the helical magnetic axis about which the helical angular shear is measured.

The helical angular velocity shear calculation used is

$$\Omega_V' = \frac{\partial}{\partial r_{hel}}\left(\frac{V_\chi}{r_{hel}}\right), \qquad (6)$$

where $V_\chi = mV_\theta + nV_\phi$ is the helical velocity and $r_{hel} = r - r_s$ is the radius measured from the location, r_s, of the surface containing the O-point or helical magnetic axis. The radius r is measured from the Shafranov-shifted axis, which is the point where the neutral beam intersects the mid-plane of the MST. Since no radial velocity information is available, the full angular velocity can only be measured at the helical angle of the tearing O-point, where contributions to the helical angular

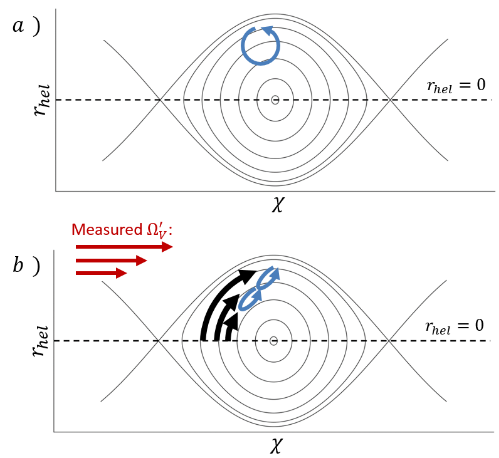

FIG. 15. Conceptual illustration of a sub-dominant tearing mode "eddy" (blue circles) projected onto the frame of reference of the dominant tearing mode island a) without shear and b) with shear. The helical angle is $\chi = m\theta + n\phi$, with the m and n modes of the dominant mode, and $r_{\text{hel}} = r - r_s$, where r_s is the radial location of the dominant mode rational surface and r is the radius. The presence of shear (black arrows) about the O-point decreases the correlation length of the sub-dominant tearing modes, breaking up the eddies.

velocity from the radial velocity is effectively zero. For the SHAx state, this corresponds to $5\phi_{\text{SHAx}} = 0$ rad, where the helical magnetic axis intersects the path of the neutral beam. The shear measurement relative to the tearing system is shown as red lines in Figure 15 b).

The critical shear necessary to suppress nonlinear energy transfer is expected to be on the order of the eddy turnover time of the sub-dominant tearing modes. The eddy turnover time for the sub-dominant modes is the sub-dominant mode angular velocity over the island width. So the critical shear must satisfy

$$\Omega_V' > \frac{\tilde{V}_{\text{sub}}}{w_{\text{sub}}^2}, \tag{7}$$

where $\tilde{V}_{\text{sub}}$ is the typical sub-dominant mode velocity and w_{sub} is the typical sub-dominant mode island width. The region between the magnetic axis and the nearest sub-dominant tearing mode is expected to be most important for establishing a shear boundary layer and disrupting nonlinear energy transfer between tearing modes. There are no measurements for sub-dominant tearing mode velocities in these 500 kA non-reversed SHAx plasmas, but previous measurements have shown sub-dominant tearing mode fluctuations to be on the order of 1 km/s in both MH and QSH reversed, 400 kA plasmas, with tearing mode widths between 5-10 cm[22]. Since the tearing mode flow is expected to be proportional to the magnetic tearing mode amplitude, and the sub-dominant magnetic tearing mode amplitudes between the 400 kA cases and the 500 kA SHAx case are comparable (on the order of a few Gauss) the measurements from the multi-helicity case provide a useful estimate for sub-dominant tearing mode flow of the SHAx case. Using these numbers as an estimate, the critical helical angular velocity shear is on the order of hundreds of thousands of $(\text{m s})^{-1}$. The maximum velocity reported was 1.5 km/s giving a maximum critical shear on the order of 6×10^5 $(\text{m s})^{-1}$.

This is the first quantitative estimate of the angular shear flow necessary to affect nonlinear energy transfer between tearing modes in this paradigm. The proposed critical shear condition is less than a previously suggested condition that a shear flow on the order of V_A/a, where V_A is the Alfvén speed and a is the minor radius, are necessary to limit nonlinear energy transfer[57]. Flows on the order of the Alfvén speed would also affect tearing modes but for a different physical reason. Flows of that speed would modify tearing mode stability itself, not the energy transfer from an unstable tearing mode to a stable one[61].

The calculation of the helical angular shear at $5\phi_{\text{SHAx}} = 0$ rad is given in Figure 16. As can be seen from the figure, the shear measured between the magnetic axis ($r_{hel} = 0$ surface) and the nearest sub-dominant tearing mode is on the order of 10^5 $(\text{m s})^{-1}$, with a measurement of shear nearest the magnetic axis close to 10^6 $(\text{m s})^{-1}$. This puts the shear in the right regime to have an effect on tearing mode energy transfer. However, the uncertainties associated with the helical angular velocity shear measurements are very large and encompass zero shear, thus the strongest statement that can be made is that shear flow cannot be ruled out as a possible effect.

Improving the resolution of the angular shear flow measurement using the same method described here depends on collecting significantly more flow data, as well as improving the estimate of the helical magnetic axis location, which was obtained from a V3FIT reconstruction of the SHAx state. The uncertainty in r_{hel} was estimated to be 2 cm, and it contributed about equally to the angular shear uncertainty as the uncertainty in the velocity. The critical shear estimate may also be modified through advancements in the theory itself, such as by including effects of three wave coupling from to the $m = 0$ mode and effects from the toroidal geometry. Improvements in estimating the eddy turnover time for a sub-dominant tearing mode beyond using the linear tearing mode island width may also change the estimate for the critical shear. Accounting for the general stochasticity of the plasma may decrease the correlation length of the plasma, increasing the critical shear estimate.

VII. SUMMARY

We have reported the first localized flow profile measurements of a self-organized non-axisymmetric plasma. This was made possible by implementing previous improvements in the absolute velocity calibration techniques on the CHERS diagnostic and mode locking control systems on MST. The axisymmetric component of the measurements show uniform toroidal flow in the plasma core, and poloidal flow with solid-body rotation on the inboard side, but peaked flow at $r/a = 0.2$

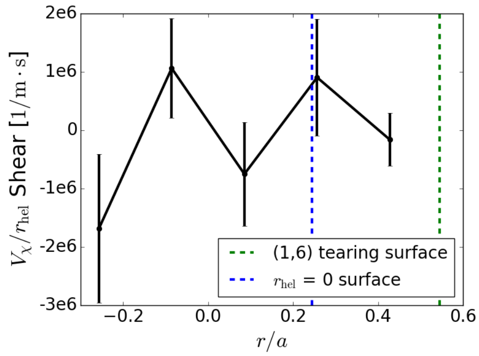

FIG. 16. Helical angular shear calculated at $5\phi_{\rm SHAx} = 0$, where the contribution to the helical angular velocity from V_r is negligible. The measurements between the surface the helical magnetic axis lies on ($r_{\rm hel} = 0$) and the nearest sub-dominant tearing mode surface are most relevant to affecting energy transfer between tearing modes. The influence of flow shear on tearing mode nonlinear energy transfer cannot be ruled out by these measurements, but no strong conclusion can be made due to the large uncertainty of the calculation.

on the outboard side. There is strong non-axisymmetry in the plasma, with $n = 5$ flows on the order of the axisymmetric flow in certain regions as well as significant $n > 5$ flow.

We have used these measurements in conjunction with new, limited periodicity, single-fluid NIMROD simulations to analyze the effects of the toroidal geometry and infer two-fluid physics in the experimental plasma flow. An inboard/outboard flow asymmetry observed in experimental data is widely attributable to the toroidal geometry of the machine. The flow asymmetry should scale with a/R_0 and could be verified with flow measurements from RFP experiments with different aspect ratios. The phase shift of the helical flow relative to the helical magnetic equilibrium is indicative of a decoupling of the ion flow from the electron flow that supports the magnetic equilibrium due to two-fluid effects.

Lastly the helical angular shear flow was characterized in the region where helical flow could be calculated and the contribution to the shear from radial velocity was minimal. Comparing the helical angular shear flow to a hypothesized critical shear necessary to disrupt energy transfer between tearing modes led to a result that is suggestive but ultimately inconclusive because of measurement uncertainties. Efforts must be made to reduce the uncertainty of both the velocity measurements and the location of the helical equilibrium relative to the velocity measurements in order to provide stronger conclusions about the importance of shear flow in SHAx formation and sustainment. A similar analysis of magnetic shear using V3FIT reconstructions, possibly requiring the implementation of SIESTA[62,63] in V3FIT, could provide valuable information about the magnetic shear in the plasma relative to a similar critical magnetic shear threshold[53].

The data and analysis presented here provide valuable information about the internal structure of SHAx plasmas, as well as a useful benchmark for future simulations. Self-consistent, toroidal, two-fluid, simulations in a parameter regime similar to experiment are likely necessary to fully understand the mechanisms responsible for QSH and eventual SHAx formation. In the future, it would be interesting to perform an analysis of the time dynamics involved in the instigation of QSH, growth, as well as in the saturated SHAx state itself. However, such an analysis would require significantly more data than that used in this paper, due to the shorter timescales of the QSH onset and growth periods.

SUPPLEMENTARY MATERIAL

The data that supports the findings of this study are available within the article and its supplementary material[64]. The supplementary material contains the digital format of the data shown in the figures in this paper.

ACKNOWLEDGEMENTS

The authors would like to thank Mark Cianciosa and James Hanson for many helpful conversations about V3FIT and VMEC. We would also like to thank Daniel Den Hartog for his advice on CHERS spectroscopy. This work was supported by the U.S. Department of Energy Office of Science, Office of Fusion Energy Sciences program, under Awards DE-FC02-05ER54814, DE-SC0018266, DE-FG02-85ER53212. This research used resources of the National Energy Research Scientific Computing Center (NERSC), a U.S. Department of Energy Office of Science User Facility operated under Contract No. DE-AC02-05CH11231.

DATA AVAILABILITY

The data that supports the findings of this study are available within the article and its supplementary material[64].

[1]T. E. Evans, R. A. Moyer, P. R. Thomas, J. G. Watkins, T. H. Osborne, J. A. Boedo, E. J. Doyle, M. E. Fenstermacher, K. H. Finken, R. J. Groebner, M. Groth, J. H. Harris, R. J. La Haye, C. J. Lasnier, S. Masuzaki, N. Ohyabu, D. G. Pretty, T. L. Rhodes, H. Reimerdes, D. L. Rudakov, M. J. Schaffer, G. Wang, and L. Zeng, "Suppression of large edge-localized modes in high-confinement DIII-D plasmas with a stochastic magnetic boundary," Phys. Rev. Lett. **92**, 235003 (2004).
[2]D. J. Ward and A. Bondeson, "Stabilization of ideal modes by resistive walls in tokamaks with plasma rotation and its effect on the beta limit," Physics of Plasmas **2**, 1570–1580 (1995), https://doi.org/10.1063/1.871307.
[3]K. Ida, N. Ohyabu, T. Morisaki, Y. Nagayama, S. Inagaki, K. Itoh, Y. Liang, K. Narihara, A. Y. Kostrioukov, B. J. Peterson, K. Tanaka, T. Tokuzawa, K. Kawahata, H. Suzuki, and A. Komori (LHD Experimental Group), "Observation of plasma flow at the magnetic island in the large helical device," Phys. Rev. Lett. **88**, 015002 (2001).
[4]K. Ida, M. Yoshinuma, H. Tsuchiya, T. Kobayashi, C. Suzuki, M. Yokoyama, A. Shimizu, K. Nagaoka, S. Inagaki, K. Itoh, and et al., "Flow damping due to stochastization of the magnetic field," Nature Communications **6**, 5816 (2015).

[5] P. Piovesan, D. Bonfiglio, M. Cianciosa, T. C. Luce, N. Z. Taylor, D. Terranova, F. Turco, R. S. Wilcox, A. Wingen, S. Cappello, C. Chrystal, D. F. Escande, C. T. Holcomb, L. Marrelli, C. Paz-Soldan, L. Piron, I. Predebon, and B. Zaniol, "Role of a continuous MHD dynamo in the formation of 3D equilibria in fusion plasmas," Nuclear Fusion **57**, 076014 (2017).

[6] P. Piovesan, V. Igochine, F. Turco, D. A. Ryan, M. R. Cianciosa, Y. Q. Liu, L. Marrelli, D. Terranova, R. S. Wilcox, A. Wingen, C. Angioni, A. Bock, C. Chrystal, I. Classen, M. Dunne, N. M. Ferraro, R. Fischer, A. Gude, C. T. Holcomb, A. Lebschy, T. C. Luce, M. Maraschek, R. McDermott, T. Odstrčil, C. Paz-Soldan, M. Reich, M. Sertoli, W. Suttrop, N. Z. Taylor, M. Weiland, M. Willensdorfer, , and and, "Impact of ideal MHD stability limits on high-beta hybrid operation," Plasma Physics and Controlled Fusion **59**, 014027 (2016).

[7] I. Chapman, M.-D. Hua, S. Pinches, R. Akers, A. Field, J. Graves, R. Hastie, and C. M. and, "Saturated ideal modes in advanced tokamak regimes in MAST," Nuclear Fusion **50**, 045007 (2010).

[8] H. Reimerdes, I. Furno, F. Hofmann, A. Martynov, A. Pochelon, and O. Sauter, "Sawtooth behaviour in highly elongated TCV plasmas," Plasma Physics and Controlled Fusion **48**, 1621–1632 (2006).

[9] E. Joffrin, A. Sips, J. Artaud, A. Becoulet, L. Bertalot, R. Budny, P. Buratti, P. Belo, C. Challis, F. Crisanti, M. de Baar, P. de Vries, C. Gormezano, C. Giroud, O. Gruber, G. Huysmans, F. Imbeaux, A. Isayama, X. Litaudon, P. Lomas, D. McDonald, Y. Na, S. Pinches, A. Staebler, T. Tala, A. Tuccillo, K.-D. Zastrow, and J.-E. C. to the Work Programme, "The 'hybrid' scenario in JET: towards its validation for ITER," Nuclear Fusion **45**, 626–634 (2005).

[10] T. Luce, M. Wade, J. Ferron, A. Hyatt, A. Kellman, J. Kinsey, R. L. Haye, C. Lasnier, M. Murakami, P. Politzer, and J. Scoville, "Stationary high-performance discharges in the DIII-d tokamak," Nuclear Fusion **43**, 321–329 (2003).

[11] W. A. Cooper, J. P. Graves, and O. Sauter, "Helical ITER hybrid scenario equilibria," Plasma Physics and Controlled Fusion **53**, 024002 (2011).

[12] R. Lorenzini, E. Martines, P. Piovesan, D. Terranova, P. Zanca, M. Zuin, A. Alfier, D. Bonfiglio, F. Bonomo, A. Canton, and et al., "Self-organized helical equilibria as a new paradigm for ohmically heated fusion plasmas," Nature Physics **5**, 570–574 (2009).

[13] S. Ortolani and D. Schnack, *The Magnetohydrodynamics of Plasma Relaxation* (World Scientific Publishing Company, 1993) p. 200.

[14] Y. L. Ho and G. G. Craddock, "Nonlinear dynamics of field maintenance and quasiperiodic relaxation in reversed-field pinches," Physics of Fluids B: Plasma Physics **3**, 721–734 (1991), https://doi.org/10.1063/1.859868.

[15] D. F. Escande, R. Paccagnella, S. Capello, C. Marchetto, and F. D'Angelo, "Chaos healing by separatrix disappearance and quasisingle helicity states of the reversed field pinch," Physical Review Letters **85**, 3169–3172 (2000).

[16] D. Clayton, B. Chapman, R. O'Connell, A. Almagri, D. Burke, C. Forest, J. Goetz, M. Kaufman, F. Bonomo, P. Franz, M. Gobbin, and P. Piovesan, "Observation of energetic electron confinement in a largely stochastic reversed-field pinch plasma," Physics of Plasmas **17**, 012505 (2010).

[17] R. Lorenzini, D. Terranova, A. Alfier, P. Innocente, E. Martines, R. Pasqualotto, and P. Zanca, "Single-helical-axis states in reversed-field-pinch plasmas," Physical Review Letters **101**, 025005 (2008).

[18] W. F. Bergerson, F. Auriemma, B. E. Chapman, W. X. Ding, P. Zanca, D. L. Brower, P. Innocente, L. Lin, R. Lorenzini, E. Martines, B. Momo, J. S. Sarff, and D. Terranova, "Bifurcation to 3d helical magnetic equilibrium in an axisymmetric toroidal device," Phys. Rev. Lett. **107**, 255001 (2011).

[19] P. Piovesan, D. Craig, L. Marrelli, S. Cappello, and P. Martin, "Measurements of the MHD dynamo in the quasi-single-helicity reversed-field pinch," Physical Review Letters **93**, 235001 (2004).

[20] F. Bonomo, D. Bonfiglio, P. Piovesan, L. Piron, B. Zaniol, S. Cappello, L. Carraro, R. Cavazzana, M. Gobbin, L. Marrelli, E. Martines, B. Momo, M. Puiatti, and M. Valisa, "Flow measurements and modelling in helical RFX-mod equilibria," Nuclear Fusion **51**, 123007 (2011).

[21] P. Piovesan, D. Bonfiglio, F. Bonomo, S. Cappello, L. Carraro, R. Cavazzana, M. Gobbin, L. Marrelli, P. Martin, E. Martines, B. Momo, L. Piron, M. E. Puiatti, A. Soppelsa, M. Valisa, P. Zanca, and B. Z. and, "Influence of external 3d magnetic fields on helical equilibrium and plasma flow in RFX-mod," Plasma Physics and Controlled Fusion **53**, 084005 (2011).

[22] D. A. Ennis, D. Craig, S. Gangadhara, J. K. Anderson, D. J. Den Hartog, F. Ebrahimi, G. Fiksel, and S. C. Prager, "Local measurements of tearing mode flows and the magnetohydrodynamic dynamo in the Madison Symmetric Torus reversed-field pinch," Physics of Plasmas **17**, 082102 (2010).

[23] L. Marrelli, P. Martin, G. Spizzo, P. Franz, B. E. Chapman, D. Craig, J. S. Sarff, T. M. Biewer, S. C. Prager, and J. C. Reardon, "Quasi-single helicity spectra in the Madison Symmetric Torus," Physics of Plasmas **9**, 2868–2871 (2002).

[24] R. Lorenzini, F. Auriemma, A. Fassina, E. Martines, D. Terranova, and F. Sattin, "Internal Transport Barrier Broadening through Subdominant Mode Stabilization in Reversed Field Pinch Plasmas," Physical Review Letters **116**, 185002 (2016).

[25] S. Munaretto, B. E. Chapman, D. J. Holly, M. D. Nornberg, R. J. Norval, D. J. Den Hartog, J. A. Goetz, and K. J. McCollam, "Control of 3D equilibria with resonant magnetic perturbations in MST," Plasma Physics and Controlled Fusion **57**, 104004 (2015).

[26] J. J. Koliner, M. R. Cianciosa, J. Boguski, J. K. Anderson, J. D. Hanson, B. E. Chapman, D. L. Brower, D. J. Den Hartog, W. X. Ding, J. R. Duff, J. A. Goetz, M. McGarry, L. A. Morton, and E. Parke, "Three dimensional equilibrium solutions for a current-carrying reversed-field pinch plasma with a close-fitting conducting shell," Physics of Plasmas **23**, 032508 (2016).

[27] F. Auriemma, P. Zanca, W. F. Bergerson, B. E. Chapman, W. X. Ding, D. L. Brower, P. Franz, P. Innocente, R. Lorenzini, B. Momo, and D. Terranova, "Magnetic reconstruction of nonaxisymmetric quasi-single-helicity configurations in the madison symmetric torus," Plasma Physics and Controlled Fusion **53**, 105006 (2011).

[28] B. E. Chapman, F. Auriemma, W. F. Bergerson, D. L. Brower, S. Cappello, D. J. D. Hartog, W. X. Ding, P. Franz, S. T. A. Kumar, P. Innocente, J.-H. Kim, L. Lin, R. Lorenzini, E. Martines, K. J. Mccollam, B. Momo, M. Nornberg, E. Parke, P. Piovesan, M. Puiatti, J. A. Reusch, J. S. Sarff, M. Spolaore, D. Terranova, P. W. Terry, and P. Zanca, "Direct Diagnosis and Parametric Dependence of 3D Helical Equilibrium in the MST RFP*," Tech. Rep. (EX/P6-01 Proceedings of IAEA Conference, 2012).

[29] J. Sarff, A. Almagri, J. Anderson, M. Borchardt, D. Carmody, K. Caspary, B. Chapman, D. D. Hartog, J. Duff, S. Eilerman, and et al., "Overview of results from the MST reversed field pinch experiment," Nuclear Fusion **53**, 104017 (2013).

[30] R. N. Dexter, D. W. Kerst, T. W. Lovell, and S. C. Prager, "The Madison Symmetric Torus," Fusion Technology **19**, 131–139 (1990).

[31] D. Craig, D. J. Den Hartog, D. A. Ennis, S. Gangadhara, and D. Holly, "High throughput spectrometer for fast localized Doppler measurements," Review of Scientific Instruments **78**, 013103 (2007).

[32] R. M. Magee, D. J. Den Hartog, G. Fiksel, S. T. A. Kumar, and D. Craig, "Toroidal charge exchange recombination spectroscopy measurements on MST," Review of Scientific Instruments **81**, 10D716 (2010).

[33] D. Ennis, *Local Measurements of Tearing Mode Flows and the MHD Dynamo in the MST Reversed-Field Pinch*, Ph.D. thesis, University of Wisconsin - Madison (2008).

[34] J. D. Hanson, S. P. Hirshman, S. F. Knowlton, L. L. Lao, E. A. Lazarus, and J. M. Shields, "V3FIT: A code for three-dimensional equilibrium reconstruction," Nuclear Fusion **49**, 075031 (2009).

[35] J. Anderson, C. Forest, T. Biewer, J. Sarff, and J. Wright, "Equilibrium reconstruction in the madison symmetric torus reversed field pinch," Nuclear Fusion **44**, 162–171 (2003).

[36] W. X. Ding, L. Lin, D. L. Brower, A. F. Almagri, B. E. Chapman, G. Fiksel, D. J. Den Hartog, and J. S. Sarff, "Kinetic stress and intrinsic flow in a toroidal plasma," Phys. Rev. Lett. **110**, 065008 (2013).

[37] B. E. Chapman, R. Fitzpatrick, D. Craig, P. Martin, and G. Spizzo, "Observation of tearing mode deceleration and locking due to eddy currents induced in a conducting shell," Physics of Plasmas **11**, 2156–2171 (2004).

[38] S. Munaretto, B. E. Chapman, M. D. Nornberg, J. Boguski, A. M. DuBois, A. F. Almagri, and J. S. Sarff, "Effect of resonant magnetic perturbations on three dimensional equilibria in the madison symmetric torus reversed-field pinch," Physics of Plasmas **23** (2016), 10.1063/1.4943524.

[39] D. Craig, E. H. Tan, B. Schott, J. K. Anderson, J. Boguski, D. J. Den Hartog, T. Nishizawa, M. D. Nornberg, and Z. A. Xing, "Intrinsic flow and tearing mode rotation in the RFP during improved confinement," Physics of Plasmas **26**, 072503 (2019).

[40] J. S. Sarff, J. K. Anderson, T. M. Biewer, D. L. Brower, B. E. Chapman, P. K. Chattopadhyay, D. Craig, B. Deng, D. J. Den Hartog, W. X. Ding, G. Fiksel, C. B. Forest, J. A. Goetz, R. O'Connell, S. C. Prager, and M. A. Thomas, "Tokamak-like confinement at high beta and low field in the re-

versed field pinch," Plasma Physics and Controlled Fusion **45**, A457–A470 (2003).

[41] M. M. Baltzer, D. Craig, D. J. Den Hartog, T. Nishizawa, and M. D. Nornberg, "Absolute wavelength calibration of a Doppler spectrometer with a custom Fabry-Perot optical system," Review of Scientific Instruments **87**, 11E509 (2016).

[42] S. Cappello and R. Paccagnella, "Nonlinear plasma evolution and sustainment in the reversed field pinch," Physics of Fluids B **4**, 611–618 (1992).

[43] Finn J, Nebel R, and Bathke C, "Single and multiple helicity Ohmic states in reversed field pinches," Physics of Plasmas **4**, 1262–1279 (1992).

[44] S. Cappello, "Bifurcation in the MHD behaviour of a self-organizing system: the reversed field pinch (RFP)," Plasma Physics and Controlled Fusion **46**, B313–B325 (2004).

[45] D. Bonfiglio, M. Veranda, S. Cappello, D. F. Escande, and L. Chacón, "Experimental-like helical self-organization in reversed-field pinch modeling," Physical Review Letters **111**, 085002 (2013).

[46] S. Cappello and D. F. Escande, "Bifurcation in viscoresistive MHD: the Hartmann number and the reversed field pinch," Physical Review Letters **85**, 3838–3841 (2000).

[47] A. F. Almagri, J. T. Chapman, C. S. Chiang, D. Craig, D. J. Den Hartog, C. C. Hegna, and S. C. Prager, "Momentum transport and flow damping in the reversed-field pinch plasma," Physics of Plasmas **5**, 3982–3985 (1998).

[48] R. Fridström, B. E. Chapman, A. F. Almagri, L. Frassinetti, P. R. Brunsell, T. Nishizawa, and J. S. Sarff, "Dependence of Perpendicular Viscosity on Magnetic Fluctuations in a Stochastic Topology," Physical Review Letters **120**, 225002 (2018).

[49] F. Ebrahimi, V. Mirnov, and S. Prager, "Momentum transport from tearing modes with shear flow," Physics of Plasmas **15** (2008), 10.1063/1.2838247.

[50] M. Veranda, D. Bonfiglio, S. Cappello, L. Chacón, and D. F. Escande, "Impact of helical boundary conditions on nonlinear 3D magnetohydrodynamic simulations of reversed-field pinch," Plasma Physics and Controlled Fusion **55**, 074015 (2013).

[51] M. Veranda, D. Bonfiglio, S. Cappello, D. F. Escande, F. Auriemma, D. Borgogno, L. Chacón, A. Fassina, P. Franz, M. Gobbin, D. Grasso, and M. E. Puiatti, "Magnetohydrodynamics modelling successfully predicts new helical states in reversed-field pinch fusion plasmas," Nuclear Fusion **57**, 116029 (2017).

[52] C. R. Sovinec, A. H. Glasser, T. A. Gianakon, D. C. Barnes, R. A. Nebel, S. E. Kruger, D. D. Schnack, S. J. Plimpton, A. Tarditi, and M. S. Chu, "Nonlinear magnetohydrodynamics simulation using high-order finite elements," Journal of Computational Physics **195**, 355–386 (2004).

[53] J. H. Kim and P. W. Terry, "Magnetic turbulence suppression by a helical mode in a cylindrical geometry," Physics of Plasmas **19**, 122304 (2012).

[54] J. R. King, C. R. Sovinec, and V. V. Mirnov, "First-order finite-Larmor-radius fluid modeling of tearing and relaxation in a plasma pinch," Physics of Plasmas **19**, 055905 (2012).

[55] W. Ding, D. Brower, D. Craig, B. H. Deng, S. C. Prager, V. Svidzinski, J. S. Sarff, W. X. Ding, V. Mirnov, G. Fiksel, and D. L. Brower, "Measurement of the Hall Dynamo Effect during Magnetic Reconnection in a High-Temperature Plasma," Physical Review Letters **93**, 045002 (2004).

[56] J. R. King, C. R. Sovinec, and V. V. Mirnov, "First-order finite-Larmor-radius effects on magnetic tearing in pinch configurations," Physics of Plasmas **18**, 042303 (2011).

[57] P. W. Terry and G. G. Whelan, "Time-dependent behavior in a transport-barrier model for the quasi-single helcity state," Plasma Physics and Controlled Fusion **56**, 094002 (2014).

[58] I. J. McKinney and P. W. Terry, "Thermal transport dynamics in the quasi-single helicity state," Physics of Plasmas **24**, 062303 (2017).

[59] H. Biglari, P. H. Diamond, and P. W. Terry, "Influence of sheared poloidal rotation on edge turbulence," Physics of Fluids B **2**, 1–4 (1990).

[60] D. Bonfiglio, F. Bonomo, P. Piovesan, L. Piron, and B. Zaniol, "Role of flow in the formation of helical states in rfx-mod," 37th EPS Conference on Plasma Physics 2010, EPS 2010 **1**, 33–36 (2010).

[61] R. Gatto, P. Terry, and C. Hegna, "Tearing mode stability with equilibrium flows in the reversed-field pinch," Nuclear Fusion **42**, 496–509 (2002).

[62] S. Hirshman, R. Sanchez, and C. Cook, "Siesta: A scalable iterative equilibrium solver for toroidal applications," Physics of Plasmas **18**, 062504–062504 (2011).

[63] M. Cianciosa, S. P. Hirshman, S. K. Seal, and M. W. Shafer, "3d equilibrium reconstruction with islands," Plasma Physics and Controlled Fusion **60**, 044017 (2018).

[64] See supplementary material at [inset link] for the digital format of the data shown in this paper.

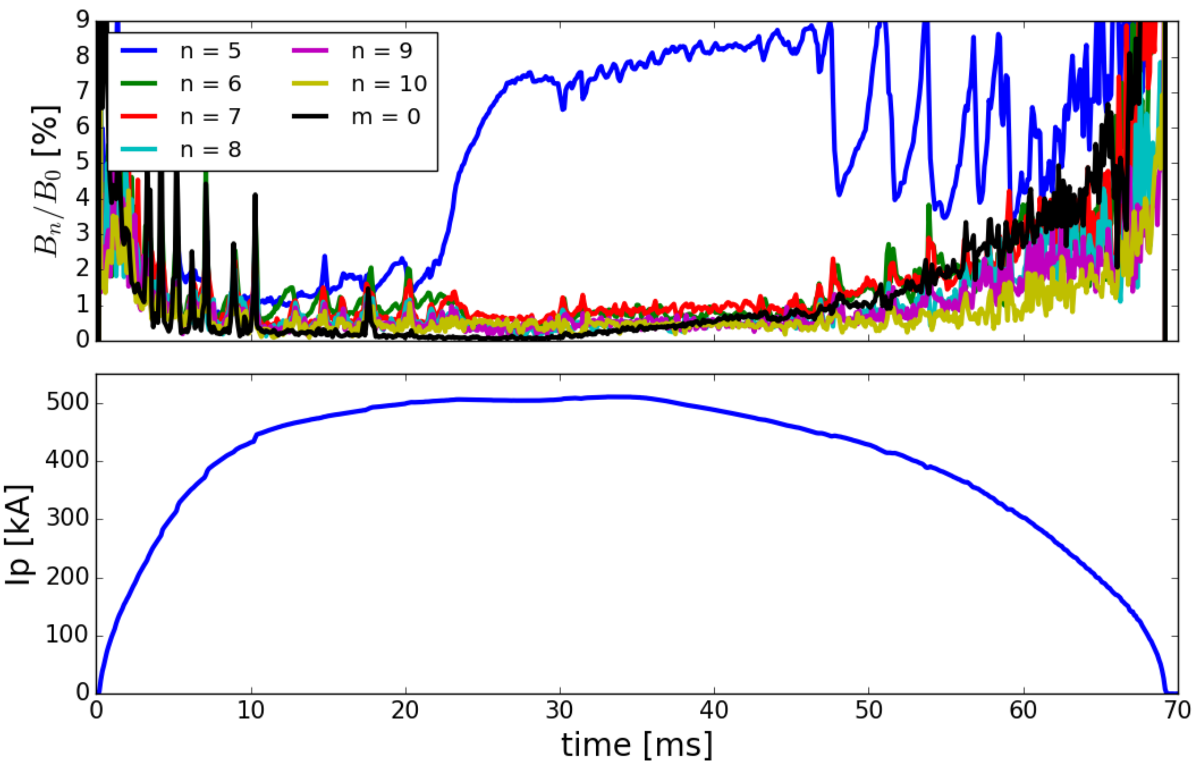
n = 5
n = 6
n = 7
n = 8
n = 9
n = 10
m = 0
B_n/B_0 [%]
Ip [kA]
time [ms]

PLEASE CITE THIS ARTICLE AS DOI: 10.1063/5.0025696

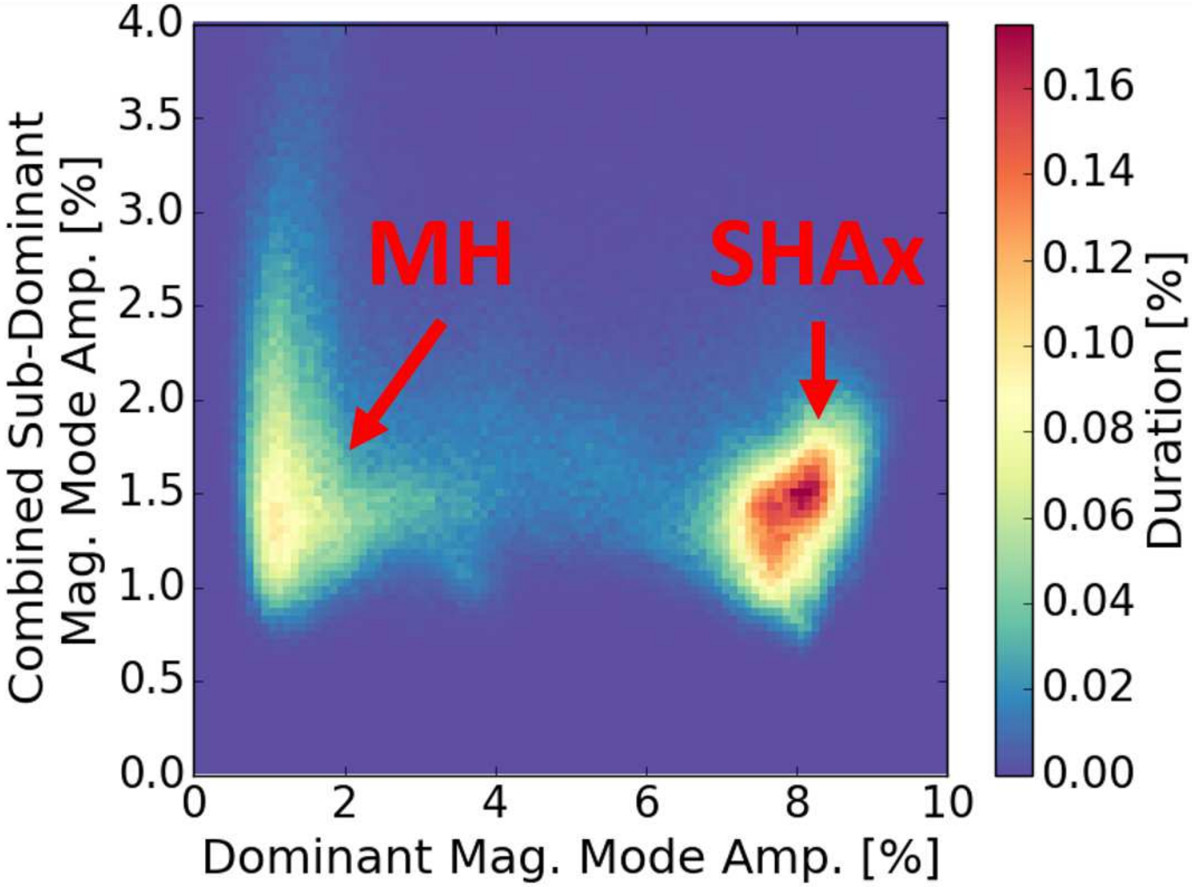

PLEASE CITE THIS ARTICLE AS DOI: 10.1063/5.0025696

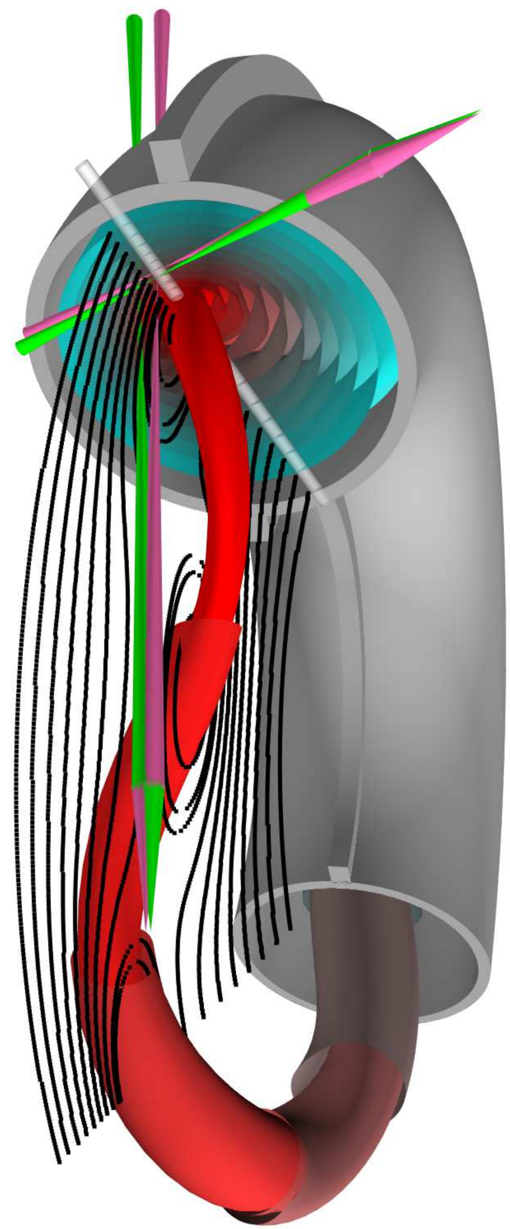

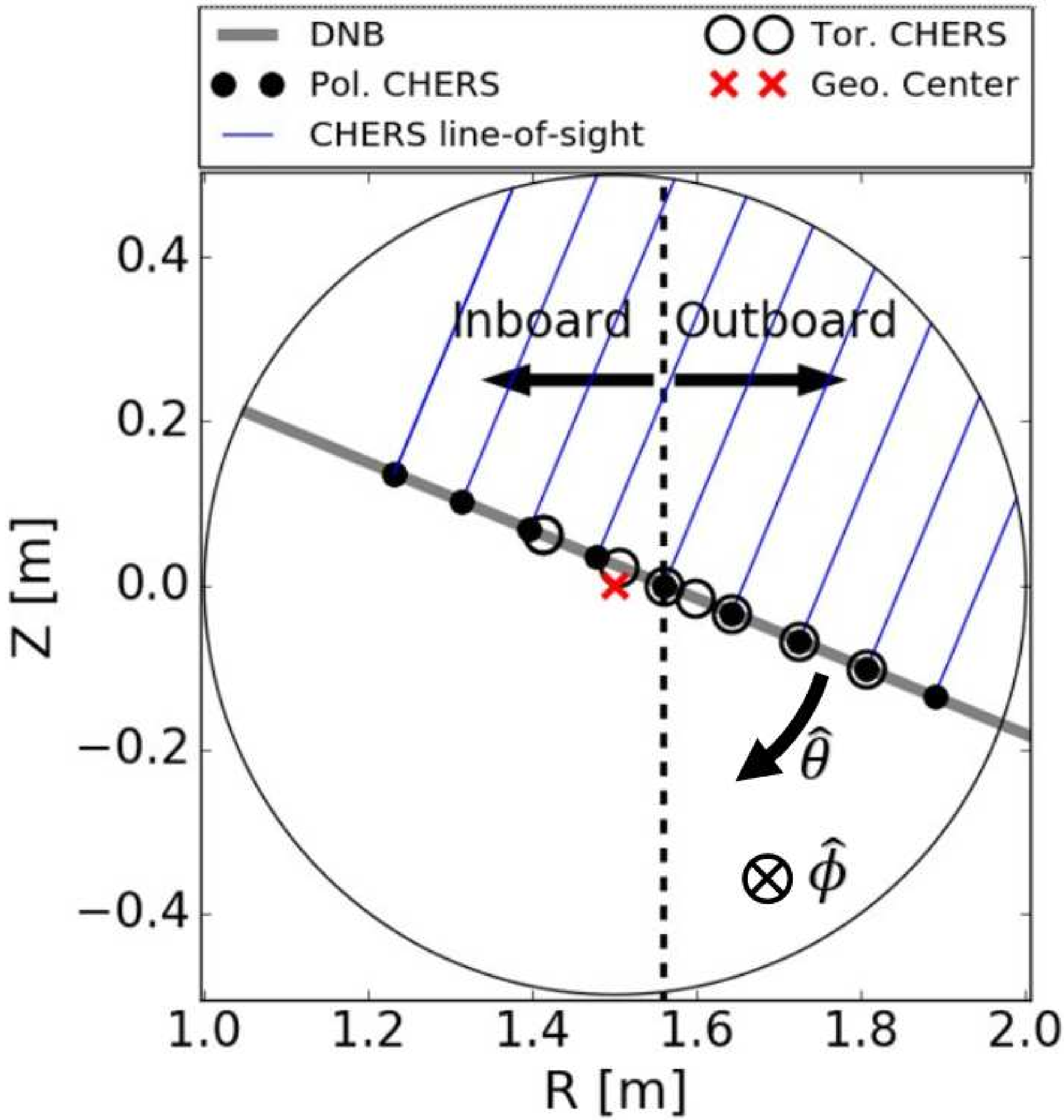
DNB
Pol. CHERS
CHERS line-of-sight
Tor. CHERS
Geo. Center
Inboard
Outboard
$\hat{\theta}$
$\otimes \hat{\phi}$
0.4
0.2
0.0
−0.2
−0.4
Z [m]
1.0
1.2
1.4
1.6
1.8
2.0
R [m]

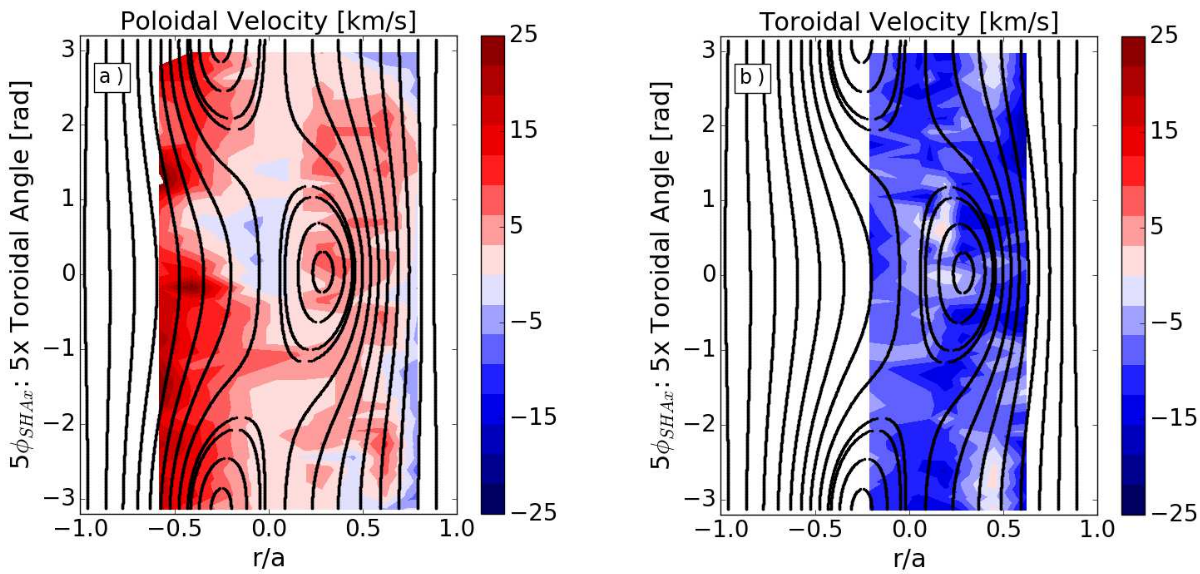
Poloidal Velocity [km/s]
a)
$5\phi_{SHAx}$: 5x Toroidal Angle [rad]
r/a
Toroidal Velocity [km/s]
b)
$5\phi_{SHAx}$: 5x Toroidal Angle [rad]
r/a

PLEASE CITE THIS ARTICLE AS DOI: 10.1063/5.0025696

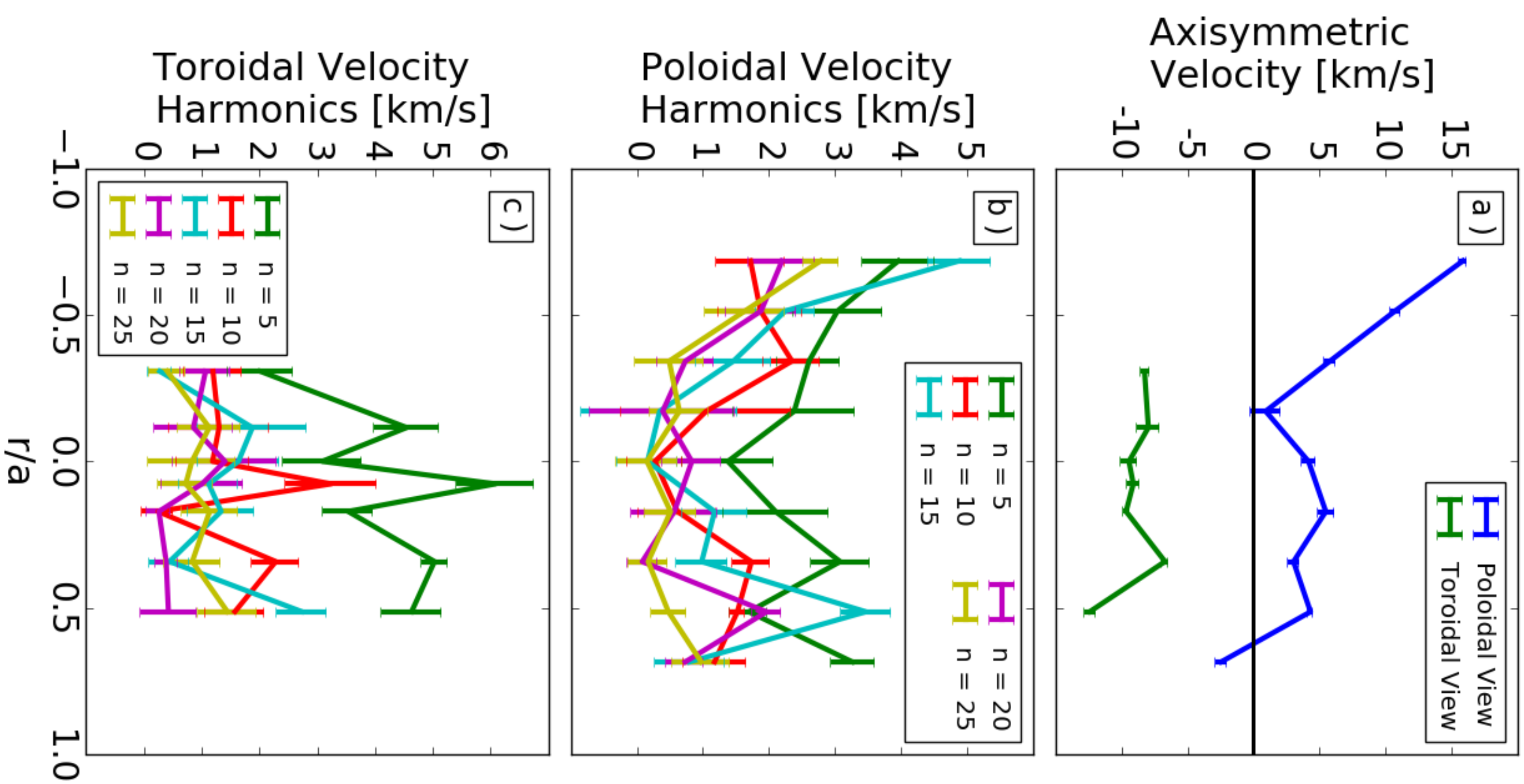

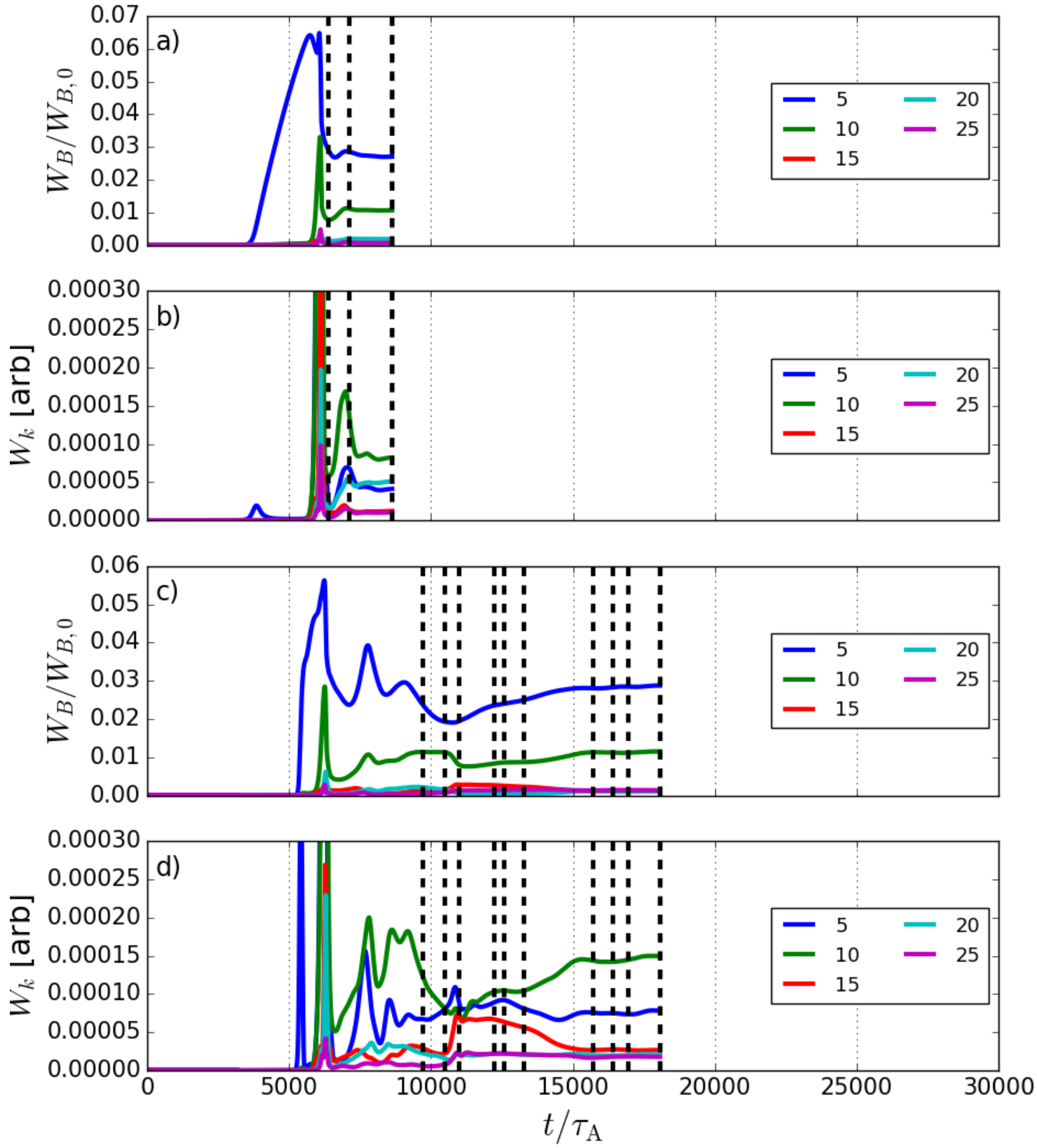
a)
b)
c)
d)
$W_B/W_{B,0}$
W_k [arb]
t/τ_A
5
10
15
20
25
0.07
0.06
0.05
0.04
0.03
0.02
0.01
0.00
0.00030
0.00025
0.00020
0.00015
0.00010
0.00005
0.00000
0
5000
10000
15000
20000
25000
30000

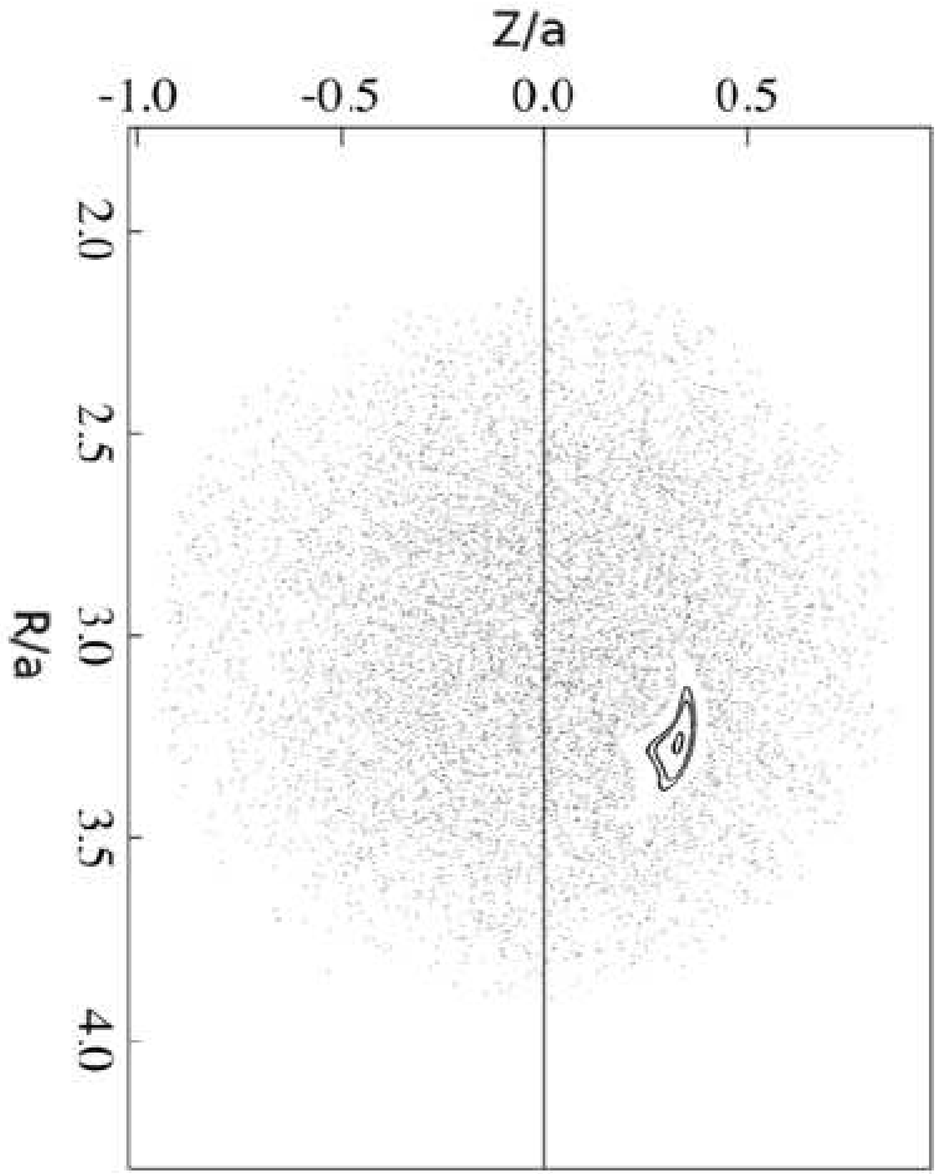
Z/a
-1.0
-0.5
0.0
0.5
R/a
2.0
2.5
3.0
3.5
4.0

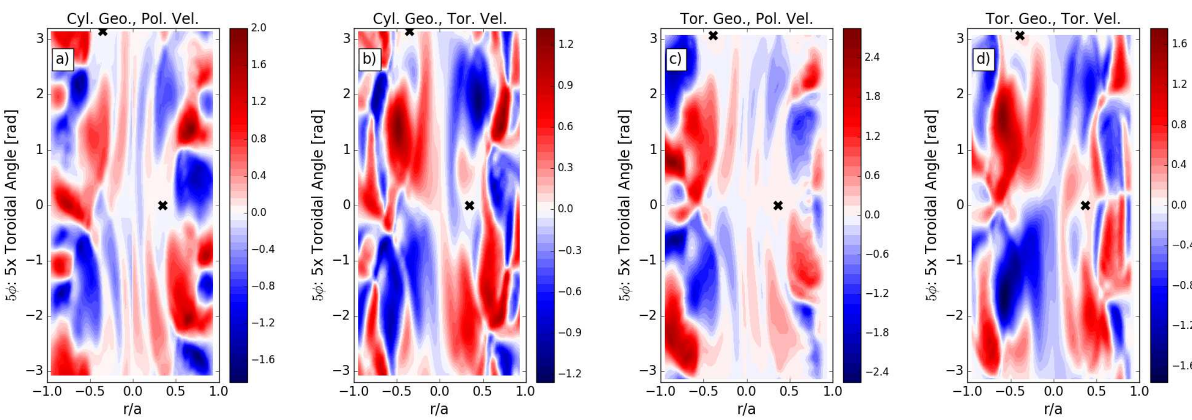
Cyl. Geo., Pol. Vel.
Cyl. Geo., Tor. Vel.
Tor. Geo., Pol. Vel.
Tor. Geo., Tor. Vel.
a)
b)
c)
d)
5φ: 5x Toroidal Angle [rad]
r/a

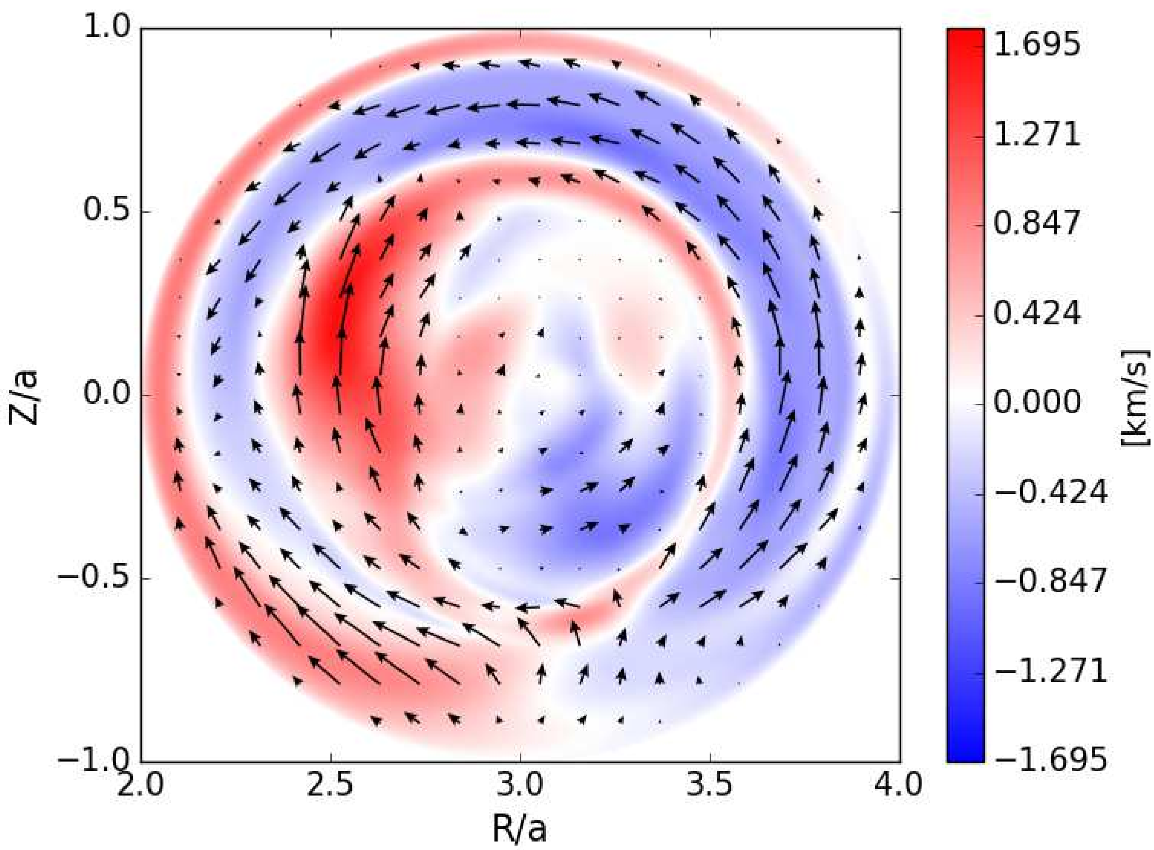
Z/a
R/a
1.0
0.5
0.0
−0.5
−1.0
2.0
2.5
3.0
3.5
4.0
1.695
1.271
0.847
0.424
0.000
−0.424
−0.847
−1.271
−1.695
[km/s]

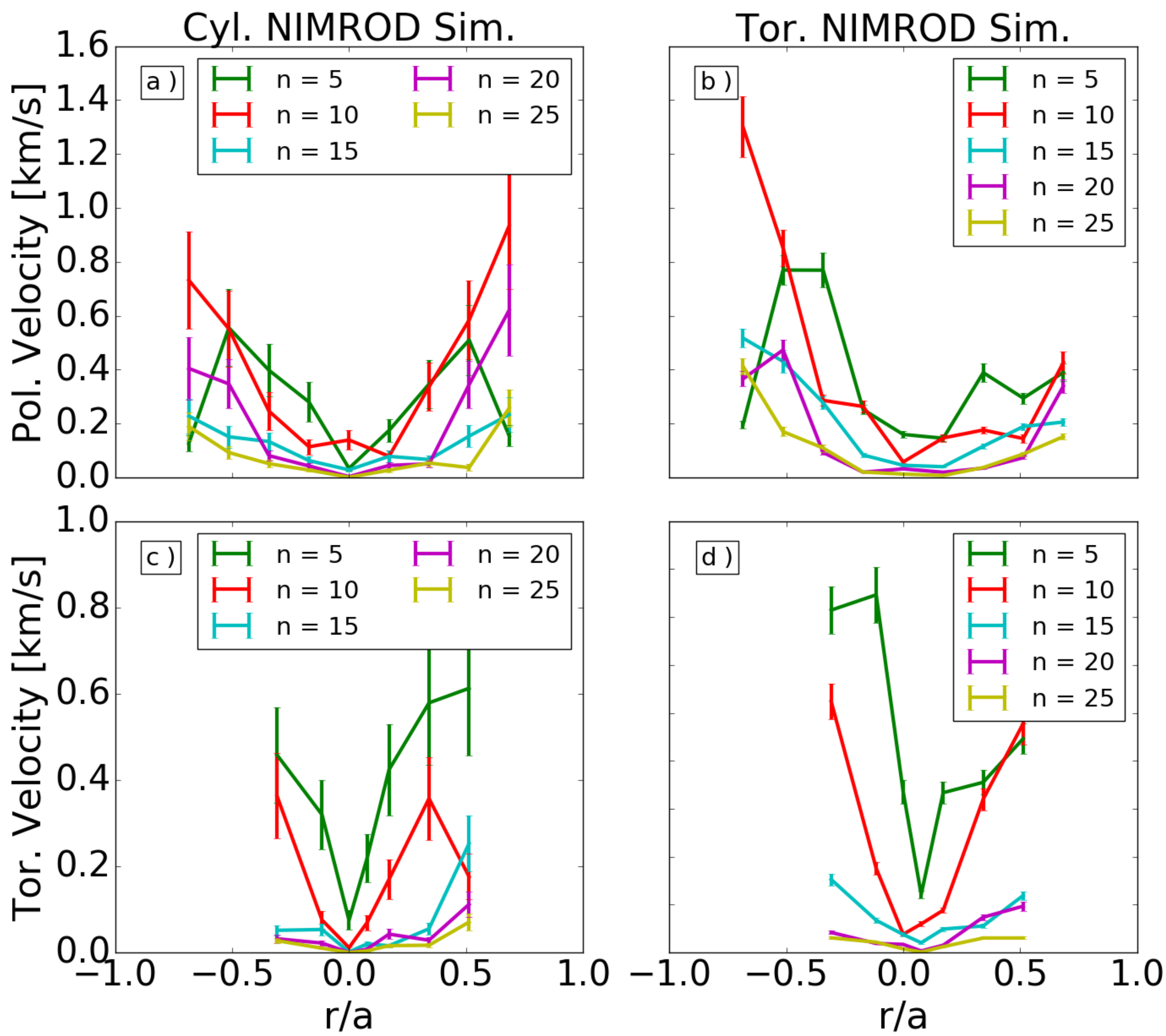
Cyl. NIMROD Sim.
Tor. NIMROD Sim.
a)
b)
c)
d)
n = 5
n = 10
n = 15
n = 20
n = 25
Pol. Velocity [km/s]
Tor. Velocity [km/s]
0.0
0.2
0.4
0.6
0.8
1.0
1.2
1.4
1.6
−1.0
−0.5
0.0
0.5
1.0
r/a
r/a

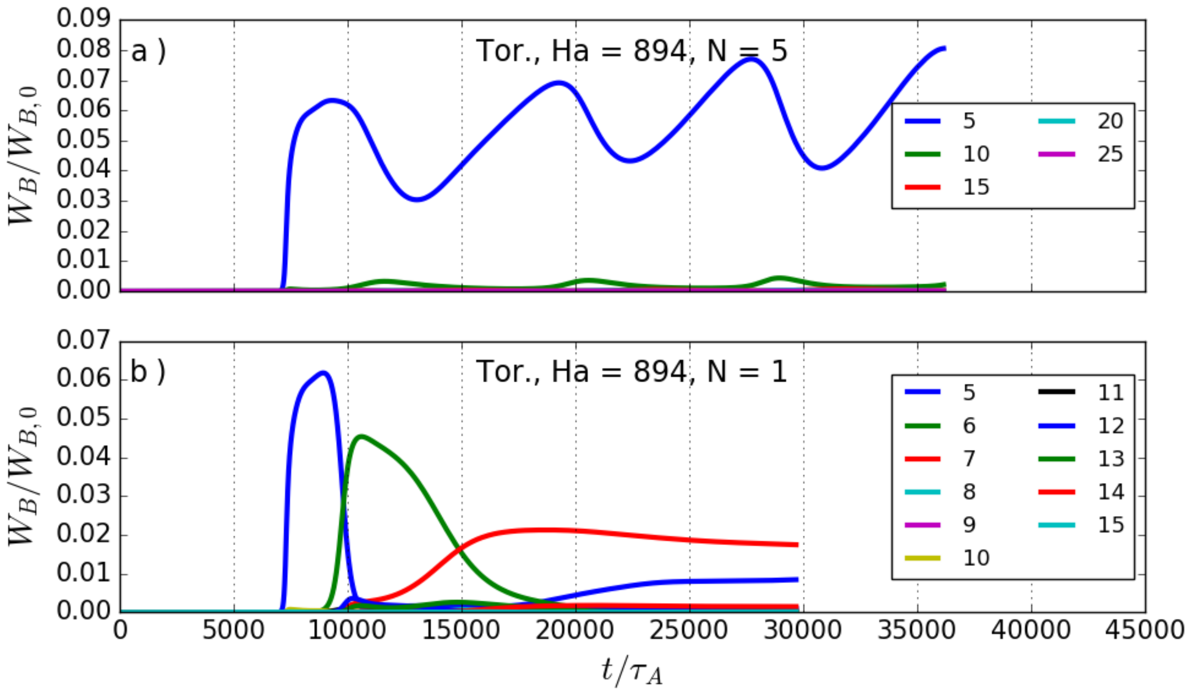
a)
Tor., Ha = 894, N = 5
5
10
15
20
25
$W_B/W_{B,0}$
b)
Tor., Ha = 894, N = 1
5
6
7
8
9
10
11
12
13
14
15
$W_B/W_{B,0}$
t/τ_A

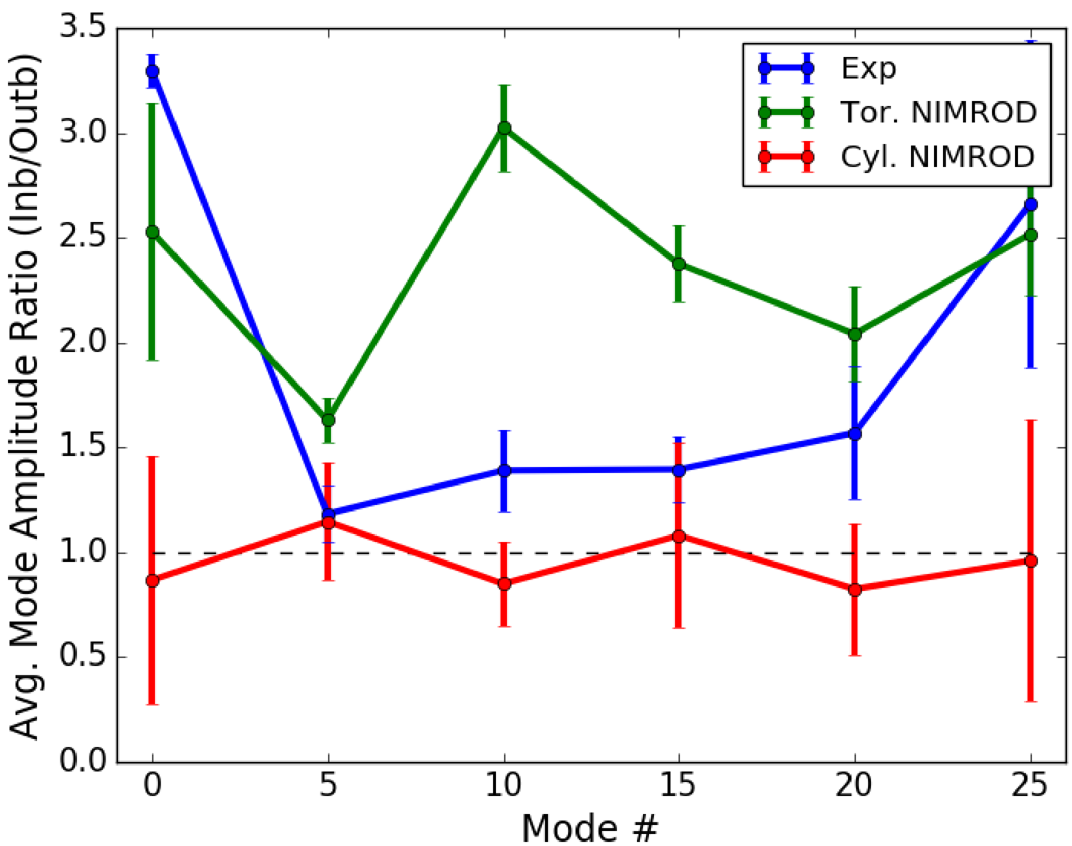
Exp
Tor. NIMROD
Cyl. NIMROD
Avg. Mode Amplitude Ratio (Inb/Outb)
Mode #
0.0
0.5
1.0
1.5
2.0
2.5
3.0
3.5
0
5
10
15
20
25

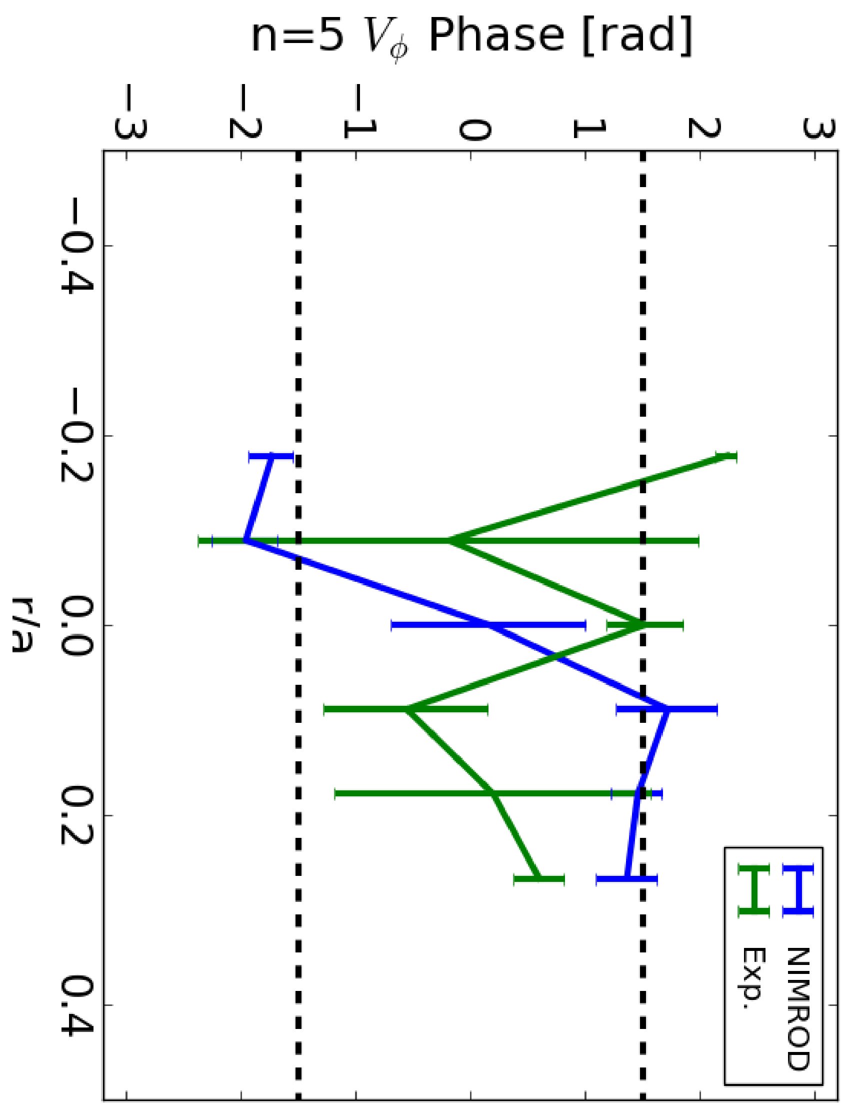
n=5 V_ϕ Phase [rad]
r/a
NIMROD
Exp.
−3
−2
−1
0
1
2
3
−0.4
−0.2
0.0
0.2
0.4

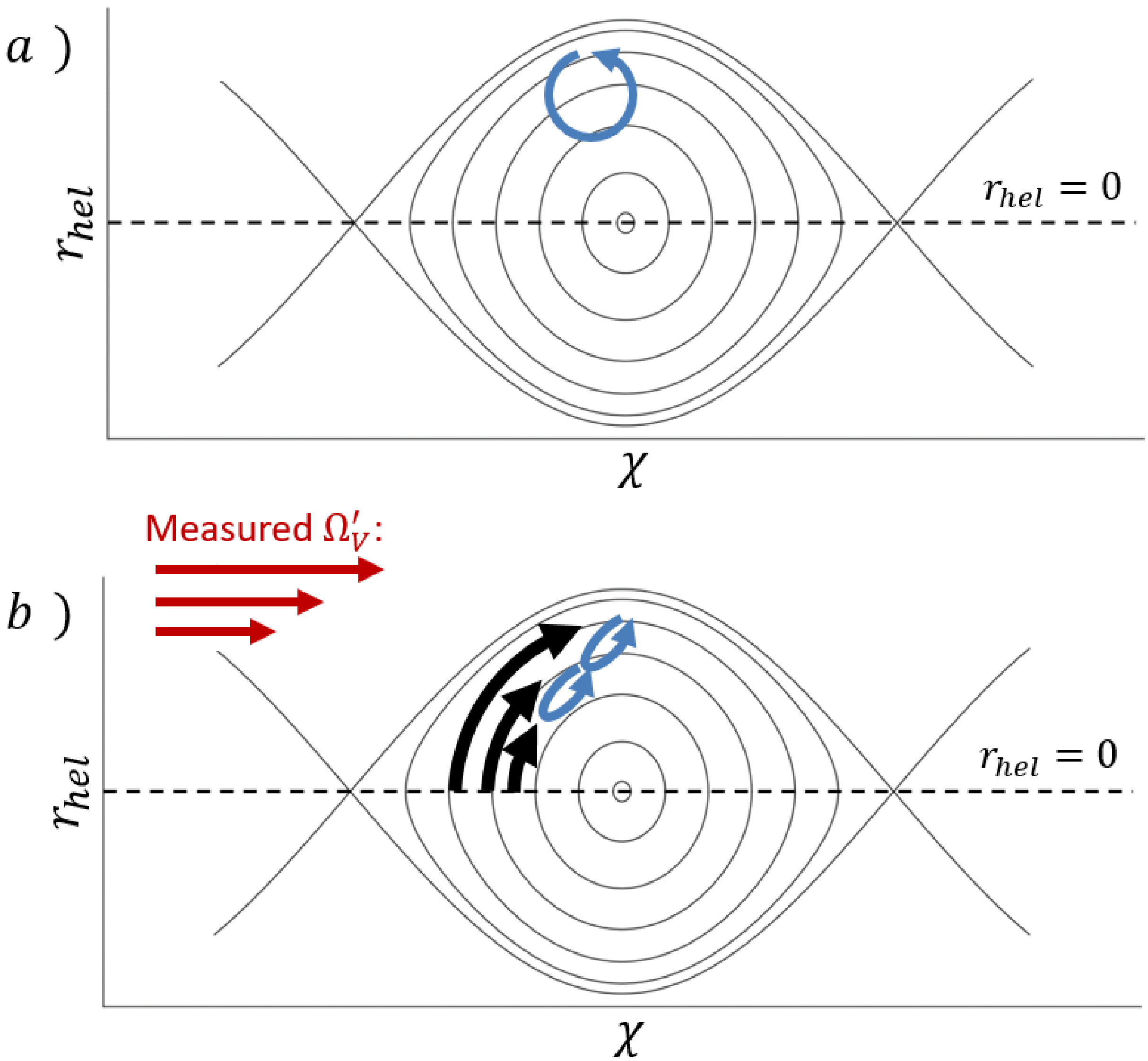
a)
r_{hel}
$r_{hel} = 0$
χ
Measured Ω_V':
b)
r_{hel}
$r_{hel} = 0$
χ

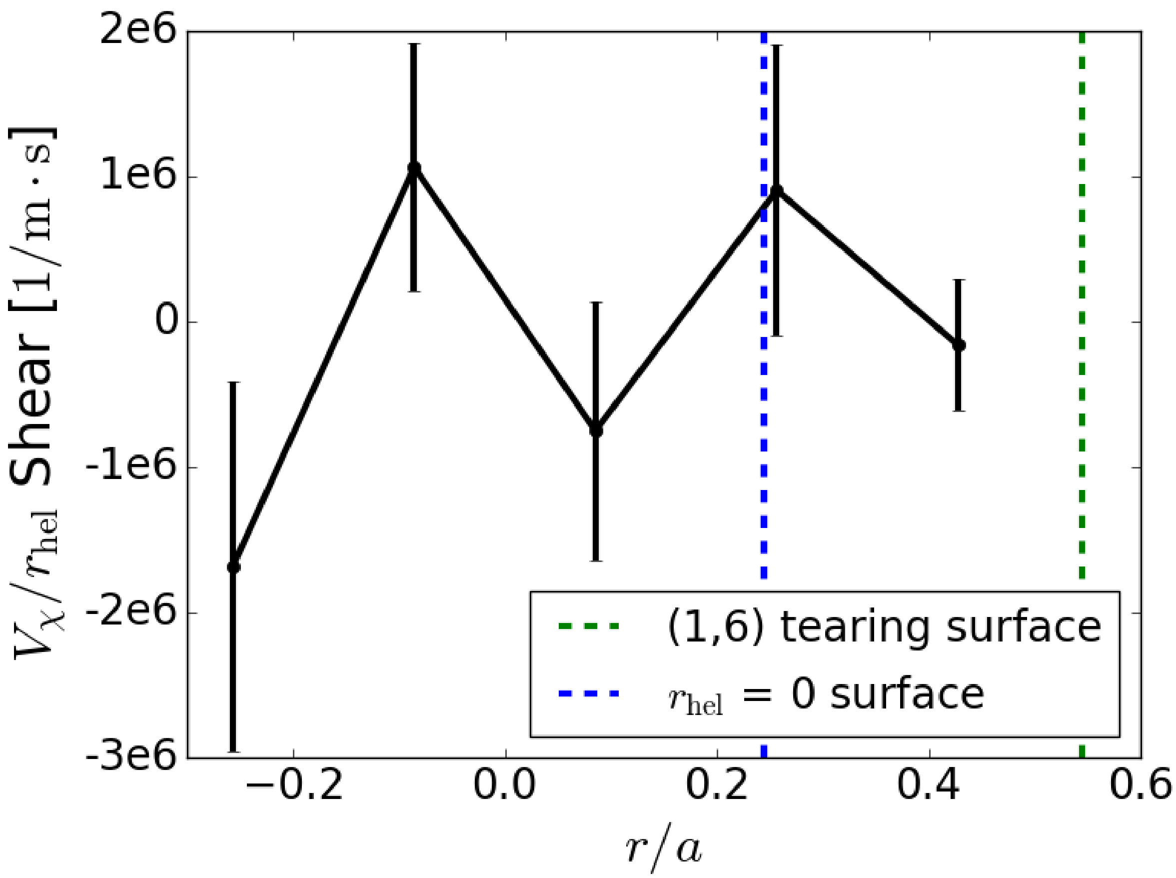
2e6
1e6
0
-1e6
-2e6
-3e6
$V_\chi/r_{\rm hel}$ Shear $[1/{\rm m}\cdot{\rm s}]$
−0.2
0.0
0.2
0.4
0.6
r/a
(1,6) tearing surface
$r_{\rm hel}$ = 0 surface